Understanding superionic conductivity in lithium and sodium salts of weakly coordinating closo-hexahalocarbaborate anions

Article

Understanding Superionic Conductivity in Lithium and Sodium Salts of Weakly Coordinating Closo-Hexahalocarbaborate Anions

Mathias Jørgensen, Patrick T. Shea, Anton W. Tomich, Joel B. Varley, Marnik Bercx, Sergio Lovera, Radovan #erný, Wei Zhou, Terrence J. Udovic, Vincent Lavallo, Torben R. Jensen, Brandon C. Wood, and Vitalie Stavila

Chem. Mater., **Just Accepted Manuscript** • DOI: 10.1021/acs.chemmater.9b04383 • Publication Date (Web): 23 Jan 2020

Understanding Superionic Conductivity in Lithium and Sodium Salts of Weakly Coordinating *Closo*-Hexahalocarbaborate Anions

Mathias Jørgensen,[a,b] Patrick T. Shea,[c] Anton W. Tomich,[d] Joel B. Varley,[c] Marnik Bercx,[e] Sergio Lovera,[d] Radovan Černý,[f] Wei Zhou,[g] Terrence J. Udovic,[g,h] Vincent Lavallo,[d] Torben R. Jensen,[a]* Brandon C. Wood,[c]* Vitalie Stavila[b]**

[a] *Interdisciplinary Nanoscience Center (iNANO) and Department of Chemistry, University of Aarhus, DK-8000 Aarhus, Denmark*

[b] *Sandia National Laboratories, Livermore, CA 94551, United States*

[c] *Materials Science Division, Lawrence Livermore National Laboratory, Livermore, CA 94551, United States*

[d] *University of California, Riverside, Riverside, 92521, California, United States*

[e] *Electron Microscopy for Materials Research, University of Antwerp, Antwerp, Belgium*

[f] *DQMP, Laboratory of Crystallography, University of Geneva, Switzerland*

[g] *National Institute of Standards and Technology, Gaithersburg, MD 20899, United States*

[h] *Department of Materials Science and Engineering, University of Maryland, College Park, MD 20742, United States*

Abstract

Solid-state ion conductors based on *closo*-polyborate anions combine high ionic conductivity with a rich array of tunable properties. Cation mobility in these systems is intimately related to the strength of the interaction with the neighboring anionic network and the energy for reorganizing the coordination polyhedra. Here, we explore such factors in solid electrolytes with two anions of the weakest coordinating ability, $[HCB_{11}H_5Cl_6]^-$ and $[HCB_{11}H_5Br_6]^-$, and a total of eleven polymorphs are identified for their lithium and sodium salts. Our approach combines *ab initio* molecular dynamics, synchrotron X-ray powder diffraction, differential scanning calorimetry, and AC impedance measurements to investigate their structures, phase-transition behavior, anion orientational mobilities, and ionic conductivities. We find that $M(HCB_{11}H_5X_6)$ (M = Li, Na, X = Cl, Br) compounds exhibit order-disorder polymorphic transitions between 203 and 305 °C, and display Li and Na superionic conductivity in the disordered state. Through detailed analysis, we illustrate how cation disordering in these compounds originates from a competitive interplay among the lattice

symmetry, the anion reorientational mobility, the geometric and electronic asymmetry of the anion, and the polarizability of the halogen atoms. These factors are compared to other *closo*-polyborate-based ion conductors to suggest guidelines for optimizing the cation-anion interaction for fast ion mobility. This study expands the known solid-state, poly(carba)borate-based materials capable of liquid-like ionic conductivities, unravels the mechanisms responsible for fast ion transport, and provides insights into the development of practical superionic solid electrolytes.

Introduction

Energy storage is widely regarded as a transformative technology for converting the electric grid to a carbon-free sustainable system and combating the effects of climate change. Solid-state batteries are an emerging option for the next-generation electrochemical devices, due to their superior safety, improved efficiency, and higher stability towards a wide range of electrode materials. However, the relatively low ionic conductivity in the solid state has proven to be a major obstacle for solid electrolyte materials, often requiring high operating temperatures in order to achieve conductivities comparable to those found in liquid electrolytes. Therefore, the discovery of new solid electrolytes has been impeded by the lack of understanding of mechanisms governing ion transport in solid state, and the complex correlations between the composition, structure, ion mobility, and electrochemical stability.[1]

Lithium and sodium compounds with weakly coordinating polyboron anions have recently gained increasing interest as solid electrolytes owing to their impressive ionic conductivity and remarkable chemical and thermal stability.[2] The excellent ionic conductivity is generally achieved by thermally induced disorder in the structure, where the large, weakly coordinating anions are free to rotate, creating an almost liquid-like environment with a constantly changing energy landscape for the cations to easily move through.[3] For instance, Li-ion conductivities of 0.15 S cm^{-1} (403 K) and 0.03 S cm^{-1} (354 K) were measured for disordered face-centered-cubic (*fcc*) $LiCB_{11}H_{12}$ and hexagonal $LiCB_9H_{10}$, respectively.[4,5] Similarly, Na-ion conductivities attain superionic values in the disordered phases of $Na_2B_{12}H_{12}$, $Na_2B_{10}H_{10}$, $NaCB_{11}H_{12}$, and $NaCB_9H_{10}$.[4–7]

Given the relative complexity of the *closo*-polyborate anions, a wealth of chemical modifications are possible, allowing for tailoring of the onset temperature for ionic conduction.[8] Currently, the transition temperatures of sodium *closo*-borate based systems range from well below room

temperature for $Na_2(CB_9H_{10})(CB_{11}H_{12})$ to around 570 °C for $Na_2B_{12}I_{12}$.[9–12] However, it is still not fully understood how specific chemical and structural modifications of the compounds alter the polymorphic transition temperature, making it challenging to rationally design materials with optimal properties. Trends derived from the growing family of metal *closo*-polyborates and derivatives suggest several factors that can affect the transition temperature and ionic conductivity of these compounds, including the crystal structure, coordination strength between anion and cation, lattice symmetry, particle size, anion mixing, and the moment of inertia of the anion.[3,13–16] In this context, the *closo*-7,8,9,10,11,12-hexahalocarbaborate anions $[HCB_{11}H_5X_6]^-$ (X = Cl, Br) are of great interest since they are extraordinarily weakly coordinating, even more so than $[CB_{11}H_{12}]^-$.[17] Figure 1 shows the distribution of Mulliken charges in the $[HCB_{11}H_5X_6]^-$ (X = Cl, Br) anions with anomalously high positive charge on apical H atoms covalently coordinated to the carbon atom, similarly to what was observed for the fully hydrogenated version of the anion $[CB_{11}H_{12}]^-$ (Figure S1, Supporting Information (SI)).[4] In $LiCB_{11}H_{12}$ and $NaCB_{11}H_{12}$, the presence of positively charged H atoms in apical positions of the *closo*-carbaborate anions has profound implications on the crystal packing, with anions oriented in a way that minimizes the interactions with the neighboring cations.

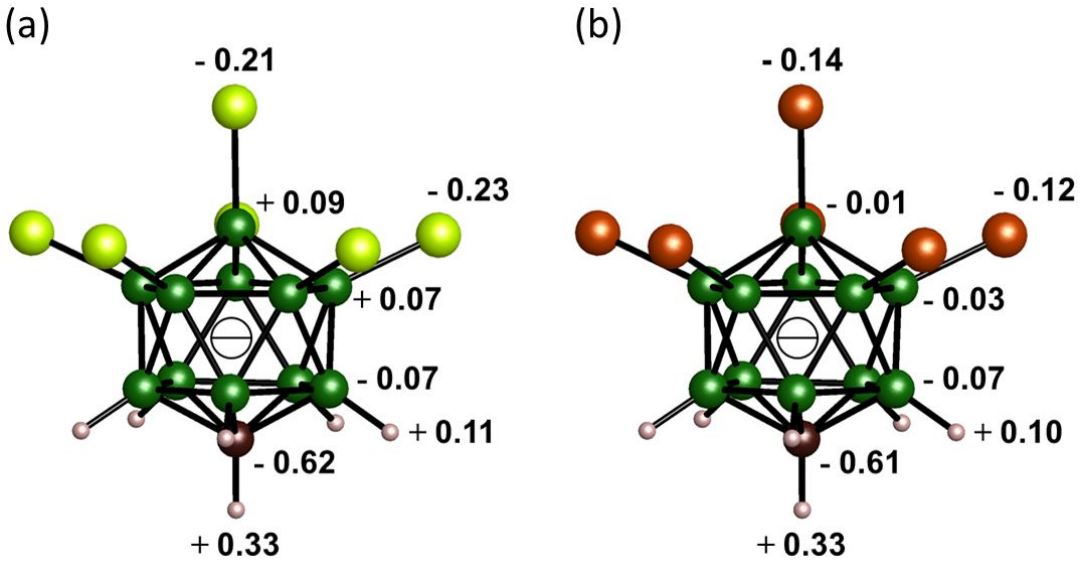

Figure 1: The *closo*-7,8,9,10,11,12-hexahalocarbaborate anions, $[HCB_{11}H_5X_6]^-$ (X = Cl (a), Br (b)), with calculated Mulliken charges.

Similarly to $[CB_{11}H_{12}]^-$, the $[HCB_{11}H_5X_6]^-$ (X = Cl, Br) anions have been extensively utilized in the stabilization of large complex cations owing to their impressive stability and weak coordination,[18] traits that are equally important for solid electrolytes. The incorporation of weakly-coordinating anions into a solid-state electrolyte is expected to enable higher ionic conductivities due to weaker interactions of the translationally diffusing cations with the anionic sublattice network. Furthermore, the unusual geometrical, chemical, and electronic anisotropy of the anion is expected to impose heavy restrictions on the crystal structure, possibly introducing significant frustration between the crystal and anion symmetry upon phase transition. In addition, the polarizable nature of the halogen atoms introduces a physical element that has not hitherto been characterized. In this work, we combine detailed structural and computational analyses to investigate the ion transport properties of lithium and sodium salts with partially halogenated *closo*-7,8,9,10,11,12-hexahalocarbaborate $[HCB_{11}H_5X_6]^-$ anions. Beyond practical applications for solid-state batteries, the rich complexity of the system provides an excellent platform for investigating key mechanistic aspects of the factors which contribute to fast ion conduction in this emerging class of solid-state electrolytes.

Experimental

All synthesis work was carried out using standard Schlenk or glovebox techniques under a dinitrogen or argon atmosphere unless otherwise stated. Dry tetrahydrofuran was obtained via distillation under argon over potassium metal and collected upon observance of the benzophenone ketyl radical. $CsHCB_{11}H_5Br_6$ and $CsHCB_{11}H_5Cl_6$ were prepared following a procedure from Reed and coworkers.[19] Trimethylammonium salts $(HNMe_3)HCB_{11}H_5Br_6$ and $(HNMe_3)HCB_{11}H_5Cl_6$ were obtained from dissolution of $CsHCB_{11}H_5Br_6$ and $CsHCB_{11}H_5Cl_6$ in hot water, followed by addition of excess trimethylamine hydrochloride to yield a white powder which was filtered hot. Unless specifically stated, reagents were purchased from commercial vendors and used without further purification. Nuclear magnetic resonance (NMR) spectroscopy was carried out using Bruker Avance NEO 400 MHz, and Bruker Avance NEO 600 MHz spectrometers.[20] HRMS was recorded on Agilent Technologies 6210 time-of-flight LC/MS using ESI technique. Fourier transform infrared (FTIR) spectra were obtained with an Agilent Cary-630 spectrometer, with an attenuated total reflectance module containing a diamond crystal. A schematic diagram of the synthesis process to isolate the $MHCB_{11}H_5X_6$ (M=Li, Na; X= Cl, Br) compounds is shown in Figure S2, SI. The starting materials and the products were comprehensively characterized by means of NMR (Figures S3–S20, SI), mass-

spectrometry (Figures S21–S22, SI), thermal analysis (Figures S23-S26, SI), X-ray diffraction (Figures S27-S37, SI), and FTIR spectroscopy (Figure S38, SI).

Synthesis of $LiHCB_{11}H_5Cl_6$: ($(HNMe_3)HCB_{11}H_5Cl_6$ (1.00 g, 2.44 mmol) was dissolved in 15 mL of THF and stirred until complete dissolution. Excess LiH was added slowly over a period of 10 min until gas evolution ceased yielding a cloudy mixture. The slurry was stirred for an additional 30 min upon which excess LiH still present in the solution was filtered to yield a clear solution. A small aliquot of the solution was dried under vacuum for analysis by ^{1}H-NMR. Reaction completion was confirmed by the absence of a singlet at 3.23 ppm in the ^{1}H-NMR spectrum corresponding to presence of the trimethylammonium cation. The reaction mixture was dried under vacuum to obtain a white powder. The product was then transferred to a side-arm Schlenk flask, and further dried at 210 °C under vacuum for multiple days until peaks at 3.64 and 1.80 ppm corresponding to THF were no longer observed by ^{1}H-NMR to yield $LiHCB_{11}H_5Cl_6$. Yields were quantitative. ^{1}H NMR (400 MHz, acetonitrile-d_3, 25 °C): δ = 3.2 – 1.2 (bm, 6H, B-H). ^{11}B[^{1}H] NMR (96 MHz, acetone-d_6, 25 °C): δ = 1.76, -4.82, -22.13 ppm. ^{11}B NMR (96 MHz, acetone-d_6, 25 °C): δ = 1.23, -5.42, -22.09, -23.37 ppm. ^{6}Li NMR (600 MHz, 25 °C): δ = 0.10 ppm. HRMS (negative mode ESI/APCI) [M].- m/z calculated = 349.6973; Observed = 348.9778.

Synthesis of $LiHCB_{11}H_5Br_6$: $(HNMe_3)HCB_{11}H_5Br_6$ **(**1.00 g, 1.478 mmol) was dissolved in 15 mL of THF and stirred until complete dissolution of the material was obtained. Excess LiH was added slowly over a period of 10 min until gas evolution ceased yielding a cloudy mixture. The slurry was stirred for an additional 30 min upon which excess LiH was filtered to yield a clear solution. A small aliquot of the solution was dried under vacuum for analysis by ^{1}H-NMR. Reaction completion was confirmed by the absence of a singlet at 3.23 ppm in the ^{1}H-NMR spectrum corresponding to presence of the trimethylammonium cation. The reaction mixture was dried under vacuum to obtain a white powder. The product was then transferred to a side-arm Schlenk flask, and further dried at 210 °C under vacuum for multiple days until peaks at 3.64 and 1.80 ppm corresponding to coordinated THF were no longer observed by ^{1}H-NMR to yield $LiHCB_{11}H_5Br_6$. Yields were quantitative. ^{1}H NMR (400 MHz, acetonitrile-d_3, 25°C): δ = 3.2 – 1.2 (bm, 6H, B-H). ^{11}B[^{1}H] NMR (96 MHz, acetone-d_6, 25°C): δ = -0.73, -8.67, -18.97 ppm. ^{11}B NMR (96 MHz, acetone-d_6, 25 °C): δ = -1.34, -9.29, -18.90, -20.19 ppm. ^{6}Li NMR (600 MHz, 25 °C): δ = -0.09 ppm. HRMS (negative mode ESI/APCI) [M].- m/z calculated = 616.4033; Observed = 616.6795.

Synthesis of $NaHCB_{11}H_5Br_6$: $NaHCB_{11}H_5Br_6$ was synthesized using a similar procedure employed for the corresponding lithium salt $LiHCB_{11}H_5Br_6$, using excess NaH instead of LiH. Yield: 100%. ^{1}H NMR (400 MHz, acetonitrile-d_3, 25 °C): δ = 3.2 – 1.2 (bm, 6H, B-H). ^{11}B[^{1}H] NMR (96 MHz, acetone-d_6, 25 °C): δ = -0.74, -8.68, -18.93 ppm. ^{11}B NMR (96 MHz, acetone-d_6, 25°C): δ = -1.35, -9.28, -18.89, -20.20 ppm. ^{23}Na NMR (600 MHz, 25 °C): δ = 3.11, -5.77 ppm. HRMS (negative mode ESI/APCI) [M].- m/z calculated = 616.4033; Observed = 616.6795.

Synthesis of $NaHCB_{11}H_5Cl_6$: $NaHCB_{11}H_5Cl_6$ was synthesized using a similar procedure employed for the corresponding lithium salt $LiHCB_{11}H_5Cl_6$, using excess NaH instead of LiH. Yield: 100%. ^{1}H NMR (400 MHz, acetonitrile-d_3, 25 °C): δ = 3.2 – 1.2 (bm, 6H, B-H). ^{11}B[^{1}H] NMR (96 MHz, acetone-d_6, 25 °C): δ = 1.08, -5.76, -23.44 ppm. ^{11}B NMR (96 MHz, acetone-d_6, 25 °C): δ = 1.09, -5.76, -22.82, -24.09 ppm. ^{23}Na NMR (600 MHz, 25 °C): δ = -5.48 ppm. HRMS (negative mode ESI/APCI) [M].- m/z calculated = 349.6973; Observed = 348.9778.

Powder X-ray diffraction and structure solution

In situ SR-PXRD data for $LiHCB_{11}H_5Cl_6$, $LiHCB_{11}H_5Br_6$, and $NaHCB_{11}H_5Br_6$ were measured at Petra III, Hamburg, at beamline P02.1 using a Perkin Elmer (XRD1621) 2D detector (λ = 0.207109 Å). *In situ* SR-PXRD data for $NaHCB_{11}H_5Cl_6$ and $NaHCB_{11}H_5Br_6$ were measured at ESRF, Grenoble, at beamline BM01 using a Multipurpose PILATUS@SNBL diffractometer (λ = 0.68663 Å).[21] Additional data were collected at ESRF, at beamline BM01 (λ = 0.78956 Å) and at Diamond Light Source, beamline I11, using a Mythen-2 Si μ-strip detector (λ = 0.824534 Å). The structures were solved *ab initio* in the program FOX,[22] using rigid bodies during the direct space parallel tempering Monte Carlo simulations. Refinement was subsequently carried out in FullProf,[23] initially retaining the rigid bodies, but ultimately refining the halogens freely and in the case of $LiHCB_{11}H_5Cl_6$ the CB_{11} cluster was allowed to move and rotate as a rigid body. Due to the relatively low scattering power of Li, manual placement of the cation was necessary. Given the crystal symmetry, *Pnma*, of the two lithium-containing compounds, three sites are possible, the 4a, 4b and 4c sites, all of which are linearly coordinated to the anion. In the 4a site, the cation is octahedrally coordinated to the negatively charged halogens, in the 4b site, it is coordinated in a square-planar manner relative to hydrogen, with Li-H distances ranging from 1.845 to 1.967 Å, while it is tetrahedrally coordinated relative to two halogens and two hydrogens in the 4c position. Comparing the Rietveld model fits, the best agreement between the model and data was found when Li was positioned in the 4a site, coordinating solely to

halogens, as expected. Temperature-dependent *in situ* XRD data was essential for identifying the different phases present in $NaHCB_{11}H_5Cl_6$ and $NaHCB_{11}H_5Br_6$ as the thermal behavior differed between the phases. This allowed for the indexing of the different polymorphs. Crystallographic data for the four compounds can be found in Tables 1 and 2.

Ionic conductivity measurements

Ionic conductivity was determined by first pressing the electrolyte powders at room temperature into pellets with 0.56 cm diameter and a thickness that ranged from 2.7 to 3.1 mm. The pellet thickness was measured using a calibrated Mitutoyo caliper. The pellets were loaded into a stainless-steel cell with 100 μm Au foil used on both sides of the pellets to make electrical contacts. The EIS spectra were collected from 0.1 Hz to 1 MHz using a Gamry600 potentiostat with a 25 mV AC signal. The EIS spectra were analyzed using Gamry software to extract the electrolyte resistance.

Thermogravimetric analysis and differential scanning calorimetry

Thermogravimetric analysis (TGA) and differential scanning calorimetry (DSC) using a Mettler TGA/DSC-1 STAR^e system were used to measure the thermal stability of the as-synthesized materials. Samples were sealed in 100-μL aluminum crucibles within the glove-box, and the TGA/DSC system punctured the crucible lid just before the measurements were made. The samples were heated from 25–500 °C with a heating rate of 5 °C/min and an Ar flow rate of 20 mL/min.

Simulation methods

Ab initio molecular dynamics (AIMD) simulations of the high-temperature superionic structure of $LiHCB_{11}H_5Cl_6$ (γ-phase, as detailed below) were performed within the Quantum Espresso code[24] using the Perdew–Burke–Ernzerhof (PBE) exchange correlation functional.[25] A plane-wave kinetic energy cutoff of 30 Ry was used for the wavefunctions and 300 Ry for the charge density and potential, as determined based on force convergence tests to within 0.05 eV/Å, and Γ-only k-point sampling was used. We employed the Car–Parrinello approach[26] with an effective electronic mass of 400 a.u. and a timestep of 8 a.u. (0.19 fs). The mass of hydrogen was set to that of deuterium in order to facilitate a larger timestep. These values were chosen based on previous studies on polyborane materials and tests ensuring negligible energy transfer between the electronic and ionic degrees of freedom.[3,13,14] Ultrasoft Rappe-Rabe-Kaxiras-Joannopoulos pseudopotentials[27] were obtained from the Quantum Espresso website. Following equilibration within a microcanonical ensemble (NVE) for

> 4 ps, production runs were performed within the canonical (NVT) ensemble for > 50 ps. To ensure proper equilibration of normal modes, Nosé–Hoover chains[28] with frequencies of 12 THz, 10 THz, and 30 THz were used for thermostating, chosen based on analysis of the vibrational density of states within our previous AIMD studies on similar materials.[3,13,14] AIMD simulations were based on 200-atom supercells of $LiHCB_{11}H_5Cl_6$. Diffusion constants (D) were evaluated by linear fits of the mean-squared displacements over the AIMD trajectories following the Einstein relation. Uncertainties were evaluated by considering the average and standard deviation of the D calculated over independent time intervals of 6 ps. Comparison analyses of the high-temperature phase of $LiCB_{11}H_{12}$ were made based on results reported by Dimitrievska *et al.*[13] Lattice constants were fixed to the experimentally measured values from the structural analysis and maintained across all simulation temperatures. The potential energy landscapes associated with isolated $LiHCB_{11}H_5Cl_6$ and $LiCB_{11}H_{12}$ molecules were computed via static density functional theory (DFT) within the NWChem code[29–32] using correlation-consistent local basis sets at the double zeta level with diffuse augmentation (aug-cc-pVDZ) as adopted previously in the analysis of the potential energy surfaces of other polyborane anions.[3,13,33,34]

Anion orientations were tracked in the AIMD simulations following the approach we first reported in work by Dimitrievska *et al.*[13] The $[HCB_{11}H_5Cl_6]^-$ anion orientations were described by quaternions $q(t)$, obtained by minimizing the deviation $\sum_i |r_i(t) - q(t) r_i^{(0)} q^{-1}(t)|^2$ between the positions $r_i(t)$ of the constituent atoms and the rotated reference positions $r_i^{(0)}$. The angle of the overall rotation of an anion over a time Δt was then computed according to $\cos[\theta(\Delta t)/2] = q(t+\Delta t) \cdot q(t)$, from which a reorientational time constant τ was extracted by fitting to the exponential decay associated with the first 25 ps of the angular autocorrelation functions. Probability densities $\rho(\theta)$ for anion orientations were solid-angle-normalized according to $\int_0^\pi \rho(\theta)(2\pi \sin\theta) d\theta = 1$. Maximally localized Wannier functions[35] were computed using the Wannier90 program[36] by sampling from every 100 AIMD frames. For each Cl and H atom, the magnitude of the vector sum of the positions of the Wannier centers associated with each atom relative to the atomic position was calculated as a measure of the polarization of the atom in response to nearby cations. For Cl, the four nearest Wannier centers to the atom were included, while for H, only the nearest Wannier center was included (see Figure S40, SI).

Results and discussion

Structural analysis

The room-temperature (RT) phases of $LiHCB_{11}H_5Cl_6$ and $LiHCB_{11}H_5Br_6$ were found to be isostructural and were solved in an orthorhombic unit cell with space group symmetry *Pnma* (62) and lattice parameters a = 11.6879(6), b = 11.1093(5), and c = 11.3771(5) Å and a = 11.7408(5), b = 11.0294(4), and c = 12.9725(6) Å, respectively (Figure 2a). This structure is referred to as the α-polymorph. The compounds are furthermore isostructural to their silver ion analog, $AgHCB_{11}H_5Br_6$.[37] A similarity between a Li and Ag compound is also found for $Li_2B_{12}H_{12}$ and $Ag_2B_{12}H_{12}$.[38] The anion packing can be described as distorted hexagonal layers in the (1 1 1) plane with an ABCABC packing sequence. Nearest-neighbor anion-anion distances range from 7.31 to 8.90 Å and 7.13 to 9.79 Å in $LiHCB_{11}H_5Cl_6$ and $LiHCB_{11}H_5Br_6$, respectively. Lithium is linearly coordinated to two $[HCB_{11}H_5Cl_6]^-$ in a zig-zag manner, forming 1-D coordination chains through the structure along the *b*-axis (Figure 2b), with a Li^+-$[HCB_{11}H_5X_6]^-$-Li^+ angle of 77.39° and 72.30° for X = Cl and Br, respectively. Both anions are coordinating in a tridentate fashion to Li through the halogens. The chains are connected through van der Waals interactions, as no obvious permanent dipole interactions are present, with the shortest intermolecular atom-atom distance being a B-X ··· H-B distance of 3.14 Å in $LiHCB_{11}H_5Cl_6$ and 3.15 Å in $LiHCB_{11}H_5Br_6$, significantly longer than their combined van der Waals (vdW) radii (2.85 and 2.95 Å, respectively). Relative to the coordinating halogen atoms, Li is coordinated in a distorted octahedral fashion, with Li-Cl distances ranging from 2.45 to 2.88 Å and Li-Br distances ranging from 2.68 to 2.91 Å.

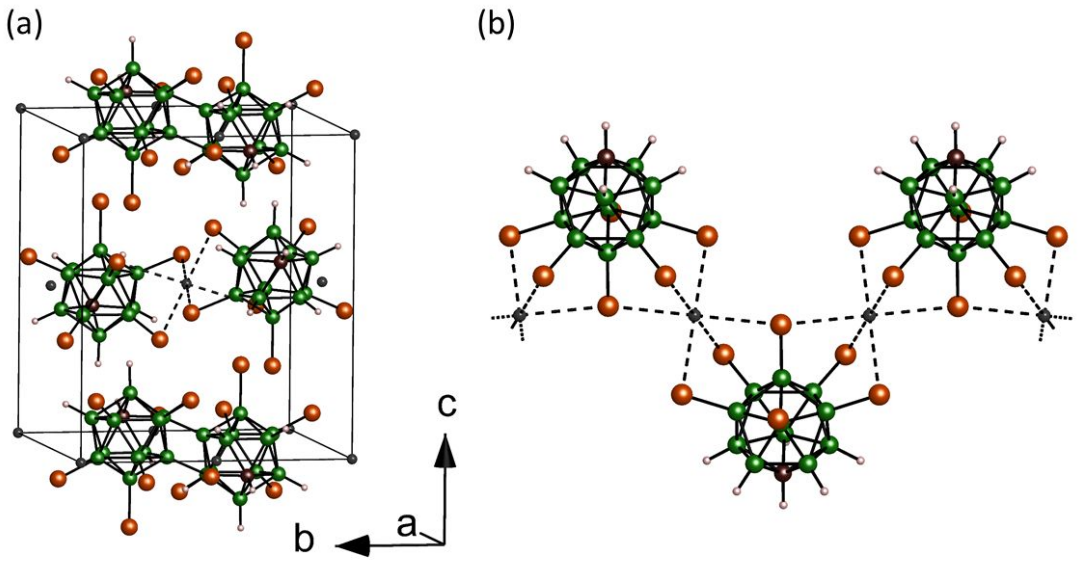

Figure 2: Representations of the structures of α-$LiHCB_{11}H_5X_6$ (X = Cl, Br): a) Orthorhombic unit cell of α-$LiHCB_{11}H_5X_6$ (X = Cl, Br); b) Chains and connectivity of $LiHCB_{11}H_5X_6$ (X = Cl, Br), showing the octahedral coordination of Li to X and the linear coordination of Li to $[HCB_{11}H_5X_6]^-$. Green: boron, dark brown: carbon, brown: X, white: hydrogen, black: lithium.

The RT structure of $NaHCB_{11}H_5Cl_6$ was solved in an orthorhombic unit cell with lattice parameters a = 12.238(2), b = 12.057(2), and c = 22.007(3) Å and space group symmetry *Pbca* (#61) (Figure 3a). The packing of the anions in the structure is *ccp*, but strongly deformed towards *hcp*. It can also be described as a layered structure of simple square-packed sheets of anions with an ABAB packing sequence (Figure 4a,b). Each AB motif is connected through trigonally coordinated Na^+ (Figure 3b) while the A and B layers are held together by interactions between the partially positively charged H on the carbon atom and a partially negatively charged Cl (H-Cl distance ≈2.66 Å compared with a combined vdW radius of 2.85 Å). The trigonal planar coordination of Na consists of two bidentate and one tridentate coordination modes to the anion, with Na-Cl distances ranging from ~2.77 to 3.40 Å. As expected from the square packing of the layers, the structure is not close packed, resulting in voids in the structure of approximately 43 $Å^3$ in size (Figure 3a, lower). These voids are large enough to accommodate small molecules such as water (~30 $Å^3$), however, the distance to the nearest Na^+ (~4.1 Å) is too long to be able to stabilize the molecule. Furthermore, introducing water into the structural model results in a worsening of the agreement between the model and the data; thus, it is concluded that these sites are unoccupied.

The full crystal structure determination of RT α-$NaHCB_{11}H_5Br_6$ was not successful, although a promising hexagonal unit cell has been determined with lattice parameters a = 15.4676(7), and b = 12.4324(7) Å. Assuming Z = 6, the volume per formula unit is ~429 Å^3 in good agreement with that of $LiHCB_{11}H_5Br_6$ (~420 Å^3) giving credibility to the indexing. The best model was achieved with a disordered hexagonal structure with space group $P6_3/m$ (Figure S39, SI), which is discussed in further detail in the Supporting Information.

Upon heating, the $MHCB_{11}H_5X_6$ (M = Li, Na, X = Cl, Br) compounds all undergo a first-order polymorphic transition into an isostructural, disordered hexagonal phase, referred to as the high-temperature (HT) γ-polymorph. The transition is accompanied by a unit cell volume expansion of approximately 5% at the transition temperature (~10% relative to RT) (except for $NaHCB_{11}H_5Cl_6$ owing to the presence of voids in the α-polymorph). Such a volume expansion is often observed for polymorphic transitions in *closo*-polyborates and their derivatives.[5,39,40] Based on symmetry considerations and systematic absences of Bragg reflections, the space group of choice is $P6_3/mmc$, with the anions centered on the 2*c* Wyckoff position (Figure 4a). In this arrangement, the anions do not show a perfect closest packing, as the distance between anions from different layers in the packing direction (along the *c*-axis) is slightly shorter than the anion-anion distance in the layers. This is reflected in the *c/a* ratio of between 1.581 - 1.600, different from the ideal 1.633, and could indicate that directionality of the anion in the crystal persists in the disordered phase, e.g. the rotation of the anion is primarily associated with a single axis. As discussed in the theory section, it turns out that the orientations somewhat favor alignment of the apical carbon atom along the [001] crystallographic axis, confirming this supposition. For comparison, the *c*/*a* ratio of the hexagonally packed $Na_2B_{12}H_{12-x}I_x$ (x ~ 0.1) is 1.64,[41] much closer to the ideal value, which is expected for the almost spherical anion.

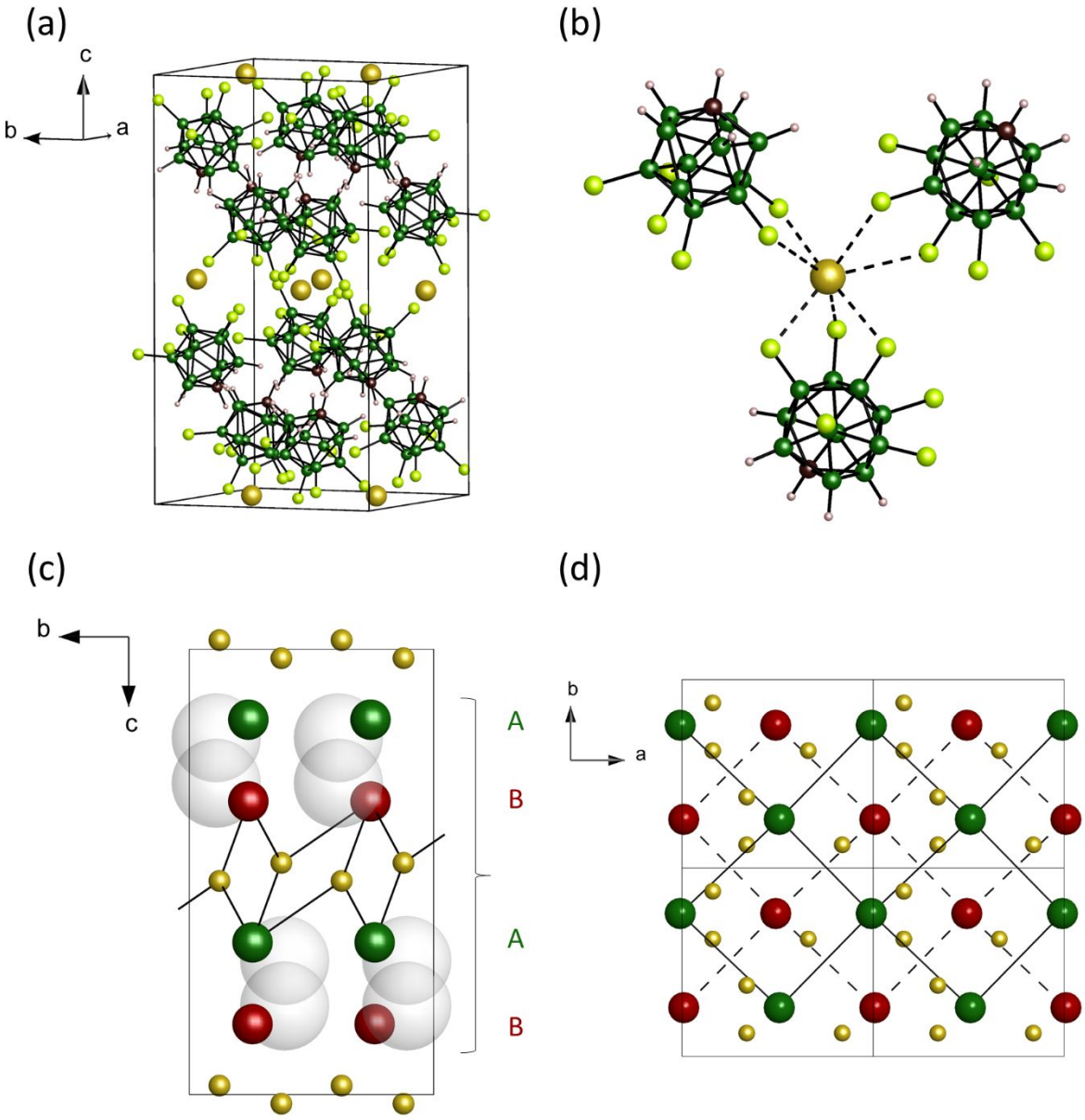

Figure 3: The structure of α-$NaHCB_{11}H_5Cl_6$. (a) Orthorhombic unit cell of α-$NaHCB_{11}H_5Cl_6$. (b) Trigonal planar coordination of a single Na^+, showing the coordination modes of the anion. (c) Simplified schematic of the layered structure. The green and red spheres represent the boron cages in layer A and B, respectively, while the grey transparent spheres represent voids in the structure. (d) A top view (seen along *c*) of four unit cells stacked together showing the square packing of the A and B layers. Green: boron, dark brown: carbon, lime: chlorine, white: hydrogen, gold: sodium.

A discrepancy between the actual and ideal hexagonal packing is observed for the hexagonally packed anions in the high-temperature polymorphs of $LiCB_9H_{10}$ and $NaCB_9H_{10}$, where the *c/a* ratio is

1.574 and 1.594, respectively,[5] indicating that the disorder of the cages is not completely random. Interestingly, the geometrically similar ellipsoidal anion $[B_{10}H_{10}]^{2-}$ packs in a *ccp* manner in the disordered high temperature polymorphs of $Na_2B_{10}H_{10}$ possibly due to a more isotropically disordered anion.[7,42] Thus, the addition of chemical anisotropy, as seen in $[CB_9H_{10}]^-$ and $[HCB_{11}H_5X_6]^-$, appears to be necessary to induce anisotropic rotation.

Comparing the α- and γ-polymorphs of the Li-based compounds, the quasi-*hcp* structure of the γ-polymorph appears to impose a less ideal linear coordination of Li^+, due to the directionality of the interaction between the cation and anion, through the halogens. Positioning Li^+ directly between two anions (i.e. bond angle anion-Li^+-anion is 180°) in the hexagonal γ-polymorph results in a Li^+-anion-Li^+ angle of 60° (slightly higher for sites between the layers in the packing direction), which is significantly lower than what is observed in the α-polymorph (72.30-77.39°) (Figure 4b). Thus, the linear site of the γ-polymorph must be distorted, likely resulting in an enthalpic penalty. This can either be achieved by moving the cation away from the linear coordination or rotating the anions slightly, compared to the conformation in the α-polymorph. The latter will, however, influence the coordination environment of the second Li^+ coordinated to the corresponding anion. Thus, the higher symmetry of the γ-polymorph (cubic vs. orthorhombic) is suggested to result in a lower stability of the Li^+ site, adding a thermodynamic penalty to the transition. The geometric frustration induced by such a mismatch between anion and crystal symmetry has previously been reported to lower the transition temperature and increase the ionic conductivity by facilitating intrinsic disorder in the structure.[13,14] This subject is discussed in further detail in the theory section (*vide infra*).

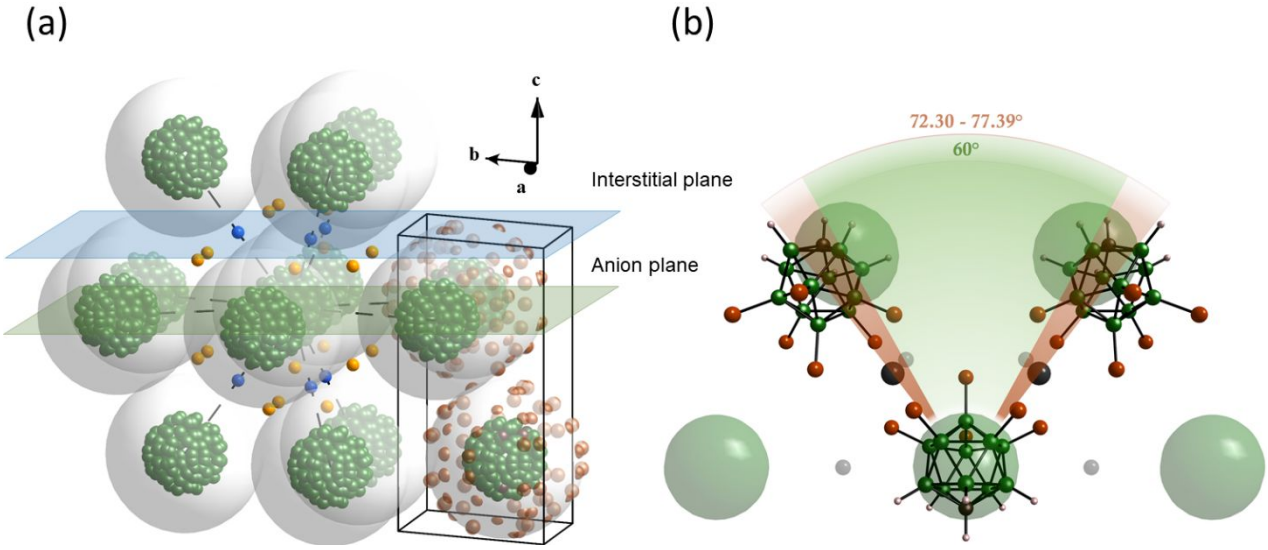

Figure 4: a) Extended disordered structure of the high-temperature γ-polymorph of $MHCB_{11}H_5X_6$ (M = Li, Na, X = Cl, Br), including the unit cell. In the interstitial plane (light blue) the blue spheres represent linear sites, while trigonal cation sites are orange. Cations in the anion plane (green) are not shown. The brown spheres represent the disordered halogen atoms. Halogens in the extended structure and H have been omitted for clarity. b) Anion-anion-anion angles in the α- (brown) and γ-polymorph (green) of $LiHCB_{11}H_5X_6$. The complex anions in the hexagonal layer of the γ-polymorph are depicted with simplified green spheres, while the Li are shown as smaller, transparent spheres manually positioned in a linear site. Green: boron; brown: X; dark grey: Li.

Table 1. Structural information on the Li-containing title compounds.

	α $LiHCB_{11}H_5Cl_6$	**β** $LiHCB_{11}H_5Cl_6$	**γ** $LiHCB_{11}H_5Cl_6$	**α** $LiHCB_{11}H_5Br_6$	**γ** $LiHCB_{11}H_5Br_6$
T (°C)[a]	100	*RT*	280	200	285
a (Å)	11.6879(6)	8.3020(3)	8.3679(4)	11.7408(5)	8.693(1)
b (Å)	11.1093(5)	12.6573(5)	-	11.0294(4)	-
c (Å)	11.3771(5)	14.3786(4)	13.392(1)	12.9725(6)	13.829(2)
V (Å^3)	1477.3(1)	1510.92(9)	812.1(1)	1679.9(1)	905.1(2)
Z	4	4	2	4	2
V/Z (Å^3)	369.31(3)	377.73(2)	406.06(5)	419.96(3)	452.6(1)
Sp. Gr.	*Pnma*	-	*P*6$_3$/*mmc*	*Pnma*	*P*6$_3$/*mmc*

[a] temperature of the scan used for Rietveld refinement.

A minor phase is present in $LiHCB_{11}H_5Cl_6$, $NaHCB_{11}H_5Cl_6$ and $NaHCB_{11}H_5Br_6$, which based on the indexing is suggested to be an orthorhombic polymorph, isostructural among the compounds. The polymorph has been denoted the β-polymorph and unit cell parameters can be found in Tables 1 and 2. Due to the low intensity of the Bragg reflections from this polymorph in all PXD data sets, the structure could not be solved. However, assuming Z = 4, the *V*/Z values for these unit cells are in good agreement with those of the α- and γ-polymorphs, giving credibility to the indexing. Furthermore, the orthorhombic unit cells approximately correspond to orthogonalizations of hexagonal unit cells with unit cell parameters close to those of the corresponding γ–polymorphs, indicating that the β-polymorph structure resembles that of the γ-polymorph, e.g., with a similar anion packing. Interestingly, a comparison of PXD data of a sample of $LiHCB_{11}H_5Cl_6$ collected one year

apart showed that the relative intensities of the Bragg peaks from the β-polymorph had increased with time, indicating that the β-polymorph is in fact the thermodynamically stable structure at RT.

Table 2: Structural information on the Na-containing title compounds.

	α $NaHCB_{11}H_5Cl_6$	**β** $NaHCB_{11}H_5Cl_6$	**γ** $NaHCB_{11}H_5Cl_6$	**α** $NaHCB_{11}H_5Br_6$ [a]	**β** $NaHCB_{11}H_5Br_6$	**γ** $NaHCB_{11}H_5Br_6$
T (°C)[b]	150	150	210	RT	-75	190
a (Å)	12.238(2)	8.32	8.3980(9)	15.4676(7)	8.59	8.7068(9)
b (Å)	12.057(2)	13.08	-	-	13.39	-
c (Å)	22.007(3)	14.49	13.386(2)	12.4324(7)	14.87	13.764(2)
V (Å^3)	3247.2(8)	1577	817.6(2)	2475.9(2)	1711	903.7(2)
Z	8	4	2	6	4	2
V/Z (Å^3)	405.9(1)	394.3	408.8(1)	412.65(3)	427.8	451.9(1)
Sp. Gr.	*Pbca*	-	$P6_3/mmc$	$P6_3/m$	-	$P6_3/mmc$

[a] based on disordered structure. [b] temperature of the scan used for Rietveld refinement.

Thermal analysis

DSC measurements for the title compounds are shown in Figure 5 and indicate reversible hysteretic phase transitions observed for most other *closo*-,[3,13–16] and *nido*-polyborates.[2] From the DSC measurements, the transition temperatures were determined to be 282, 305, 203, and 218 °C, for $LiHCB_{11}H_5Cl_6$, $LiHCB_{11}H_5Br_6$, $NaHCB_{11}H_5Cl_6$, and $NaHCB_{11}H_5Br_6$, respectively, with reversible endothermic features during heating and exothermic features upon cooling for at least three cycles. Based on the TGA results (Figures S23-S26 and accompanying text in the SI), the compounds show exceptional thermal stability above their transition temperature, with decomposition temperatures ranging from 400 to 440 °C (based on the onset temperature of mass loss), making them of potential interest for high-temperature battery applications. Upon cooling, the compounds show hysteresis when reverting to the RT structures, ranging from ~35 °C in $NaHCB_{11}H_5Br_6$ to ~115 °C in $NaHCB_{11}H_5Br_6$. Notably, the hysteresis of the β → γ → β transitions of $LiHCB_{11}H_5Cl_6$ and $NaHCB_{11}H_5Cl_6$ (Figures 5a and 5c) is smaller than for the α → γ → α transition, supporting a higher

structural similarity between the β- and γ- polymorphs compared to the α- and γ-polymorphs. The significant hysteresis observed for $NaHCB_{11}H_5Cl_6$ is suggested to be due to the structural difference between the α- and γ-polymorph, which do not share an overall anion packing, as it is otherwise the case for $LiHCB_{11}H_5Cl_6$ and $LiHCB_{11}H_5Br_6$. Thus, the structural rearrangement reverting to the RT structure is more complex. However, this does not explain the large hysteresis also observed for the β/γ-transition.

For $LiHCB_{11}H_5Cl_6$ the β → γ and α → γ, as well as the γ → α and γ → β (Figure 5a), transitions are clearly distinguishable at 245, 282, 235 and 225 °C, respectively, while in $NaHCB_{11}H_5Cl_6$, the transitions are only distinguishable upon cooling (Figure 5c). The transitions γ → α and γ → β are observed at 85 and 110 °C (~150 and 125 °C from *in situ* PXD), respectively. Interestingly, the relative DSC signals of the γ → α and γ → β transitions in $NaHCB_{11}H_5Cl_6$ change with every cycle, resulting in the γ → β transition dominating. The preferred transition could be particle size-dependent, thus as the particles grow during heat treatment, the preference shifts from α to β.

During heating and cooling of $LiHCB_{11}H_5Br_6$ and $NaHCB_{11}H_5Br_6$, only one reversible event is distinguishable. For $LiHCB_{11}H_5Br_6$, this agrees with the PXD data. However, for $NaHCB_{11}H_5Br_6$, two events were observed in the *in situ* PXD data during cooling. Further discrepancy between the DSC data and the *in situ* PXD data was noted for all samples as the similar intensities of endothermic and exothermic events indicate full polymorphic conversion, in contrast with observations based on the *in situ* PXD data (Figures S27, S30, S32, SI). Here the conversion back to the α-polymorph was generally sluggish and only small amounts of the α-polymorph were present at RT after cooling. *Ex situ* measurements of just-cooled samples at RT do not contain any of the HT polymorph; thus, it could be an effect of the sample environment during the PXD measurement.

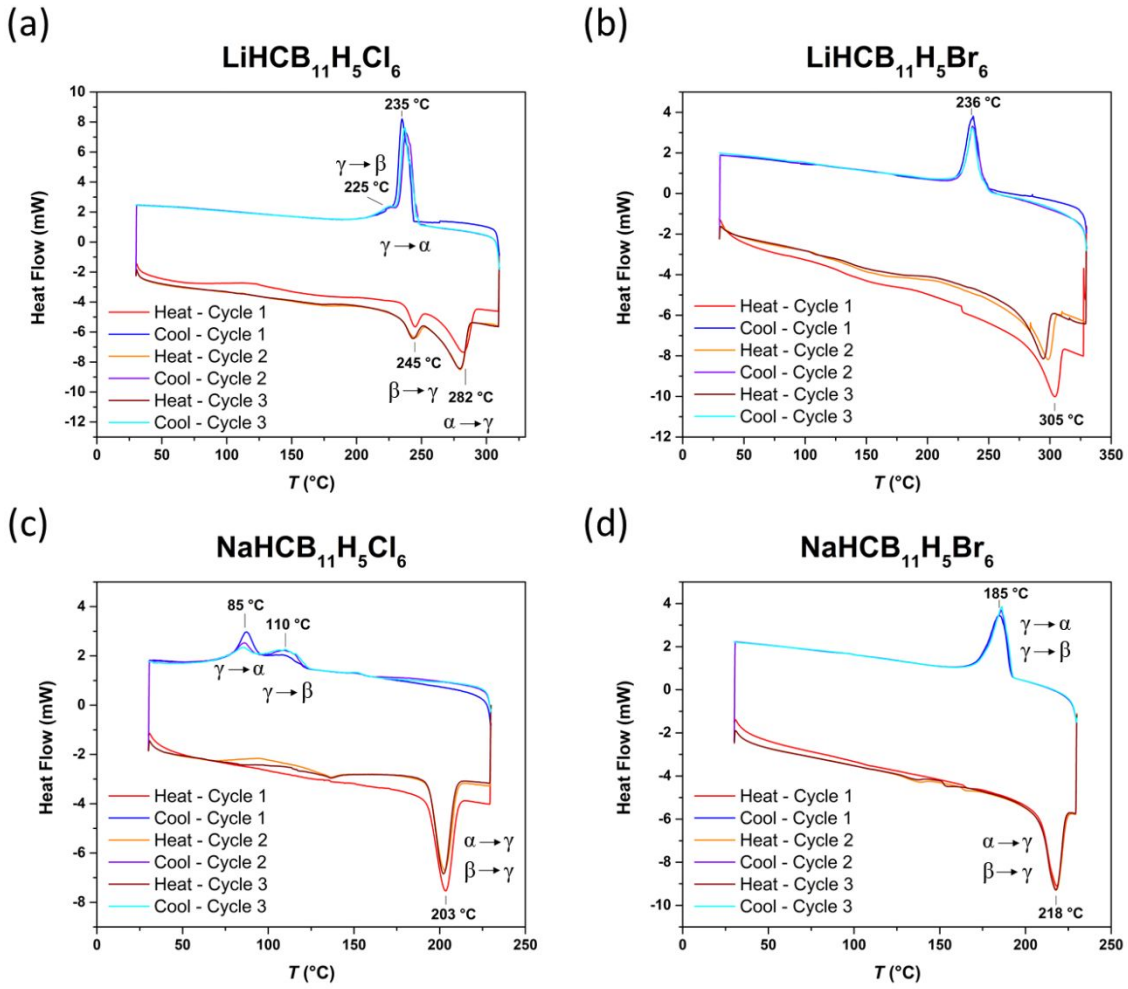

Figure 5: DSC measurements of the four title compounds using a heating rate of 5 °C/min under a flow of argon. (a) $LiHCB_{11}H_5Cl_6$. (b) $LiHCB_{11}H_5Br_6$. (c) $NaHCB_{11}H_5Cl_6$. (d) $NaHCB_{11}H_5Br_6$.

Ionic conductivity

Figure 6 shows the results from tests of Li^+ and Na^+ ion conductivity of solids with weakly coordinating $[HCB_{11}H_5X_6]^-$ (X = Cl, Br) anions. As is the case for other *closo*-(carba)borates, the ionic conductivities of the title compounds increase by orders of magnitude upon undergoing their order-disorder polymorphic transition. These conductivities reach impressive values of 6 - 35 $mS \cdot cm^{-1}$, approaching those measured for $Na_2B_{12}H_{12}$ and Na β-alumina.[6,43] The activation energies for conductivity, determined based on the slope of $\ln(\sigma T) = \ln(A) + E_a/(k_b T)$, range from ~300 meV to 380 meV in the high-temperature region. This is close to the values reported for other *closo*-(carba)borates, e.g., 220 meV for $NaCB_{11}H_{12}$ and $LiCB_{11}H_{12}$ and 470 meV for $Na_2B_{10}H_{10}$.[4,7]

Interestingly, even for the RT structures, the activation energies are relatively low, ranging from 430 to 530 meV—not substantially higher than those at HT and similar to the RT activation energies of 409 meV found for RT $LiCB_{11}H_{12}$ and $NaCB_{11}H_{12}$.[44] Conventionally, activation energies for ion conduction have contributions from both the formation and migration of mobile defects. At RT, the structure is ordered, so non-negligible contributions from defect formation are expected. Nevertheless, the activation energies calculated for the title compounds in the RT structure are far lower than typical defect formation energies for ionic crystals (for comparison, the formation energy of Frenkel defects in AgCl is ~1.45 eV and of Schottky defects in NaCl is ~2.44 eV).[45,46] This may reflect the weakly coordinating nature of the anions within the RT structures, which facilitates defect formation. Alternatively, ionic conductivity in the low-temperature regime may be a result of extrinsic disorder from cation impurities or frozen-in, high-energy defects from the HT polymorph. This is supported by the change in slope observed well before the HT polymorph, which is often related to a shift from primarily extrinsic to intrinsic contributions to the charge carrier concentration. For example, in $NaHCB_{11}H_5Cl_6$, the change in slope occurs approximately 25 °C below the onset of the polymorphic transition. The activation energy in this intermediate region was estimated to be 2.9 eV, which is consistent with the values observed for other ionic crystals.

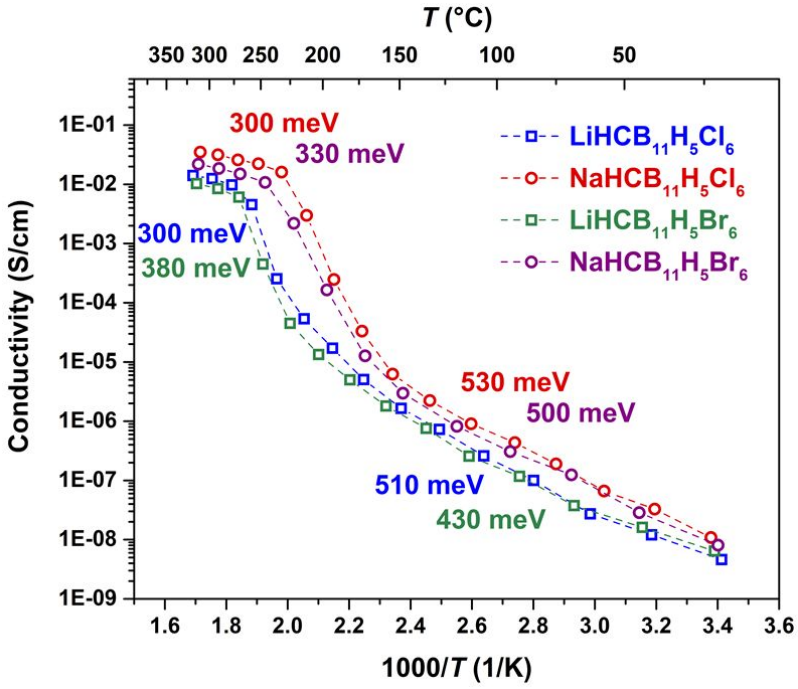

Figure 6: Ionic conductivity upon heating of pressed pellets of $M(HCB_{11}H_5X_6)$ (M = Li, Na; X = Cl, Br) solid electrolytes as a function of inverse temperature.

Trends in the order-disorder transition

The chemical and structural diversity of *closo*-poly(carba)borates creates opportunities to systematically tune the temperature of the observed order-disorder polymorphic transitions, which in turn allows fine control over ionic conductivity in a wide temperature range. Prior experimental and theoretical results have revealed complex interdependencies in the observed trends of Li^+ and Na^+ ion conductivity as a function of carbon substitution in the boron cage, lattice expansion, cation substitution, and molecular weight of the anion.[3,4,13–15,47–50] Our results contribute a new factor to this discussion—namely, the partial and specific substitution of halogen atoms for hydrogen in the anion. The halogen atoms are expected to have several impacts, including increased molecular weight, electronegativity, and polarizability.

Figure 7 shows the order-disorder transition temperatures plotted as a function of the molecular weight of the anion for known Li and Na *closo*-borates and *closo*-carbaborates, including the compounds in the current study. First, it is seen that lithium and/or divalent anion-based compounds, have higher transition temperatures relative to their sodium and monovalent anion counterparts. This could reflect a stronger coordination interaction, leading to a higher stability of the ordered (LT) structure and reduced ion mobility. Second, for salts of the same cation and nominal charge of the anion, heavier anions yield higher order-disorder transition temperatures. This can be justified in terms of the larger moment of inertia, which may reduce the rate of reorientation dynamics associated with the disorder transition. Thus, despite $[HCB_{11}H_5X_6]^-$ (X = Cl, Br) anions reportedly being more weakly coordinating than non-halogenated carbaborates,[17] which should reduce the transition temperature, the effect appears to be offset by the factor of the increased mass of the bulkier anion. However, these simplistic observations are insufficient to adequately explain all details of the data in Figure 7. For instance, sharp increases in the transition temperature are observed upon halogenation of *closo*-(carba)borates compared to non-halogenated *closo*-(carba)borates, yet further increases in mass upon substitution with far heavier halogens have a relatively minor effect. This suggests that the actual trends in ionic conductivity are a result of a more complex interplay between several factors. We explore several of these in further detail using high-fidelity quantum simulations of the $LiHCB_{11}H_5Cl_6$ system, as described below.

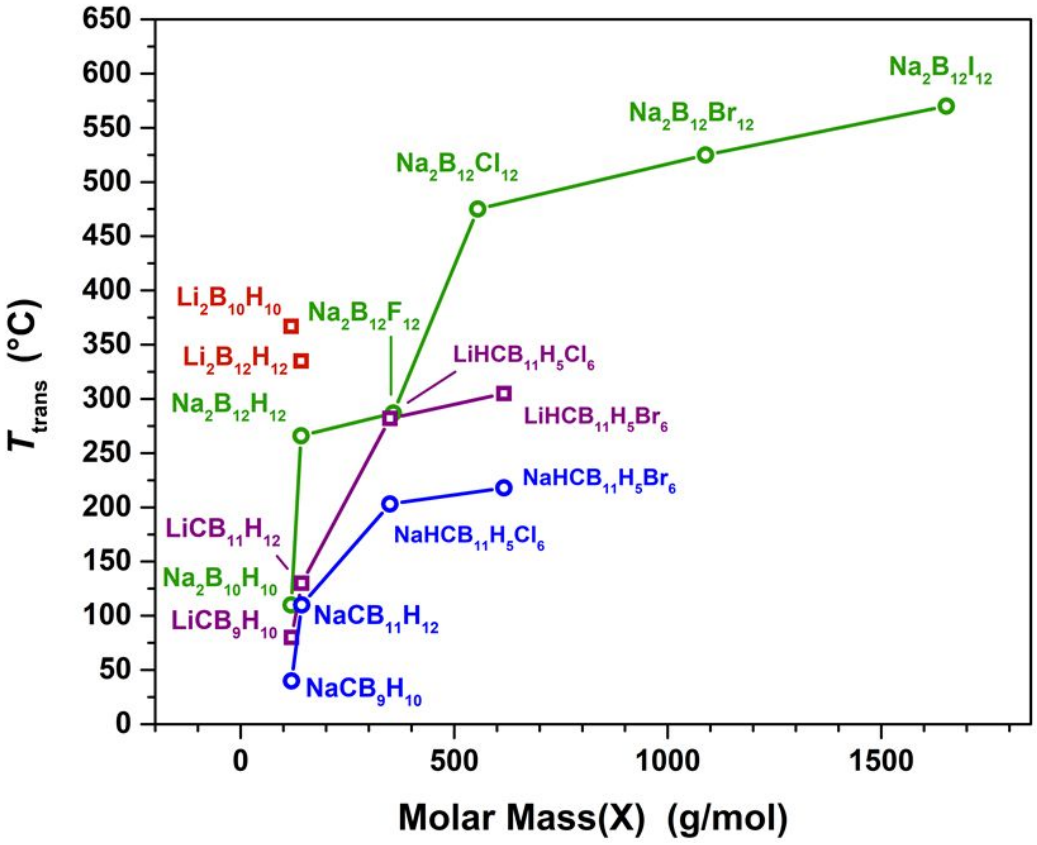

Figure 7: The polymorphic transition temperatures (upon heating) of the known Li- and Na-*closo*-(carba)borates as a function of the molar mass of the anion, showing a trend of higher transition temperatures with increasing mass.[4,5,7,10,11,39,40,51,52]

DFT and *ab initio* MD simulations

To more completely investigate the nature of the anion-cation interactions, we further performed extensive DFT and AIMD simulations on the representative example of $LiHCB_{11}H_5Cl_6$. In our previous simulation work on $[B_{12}H_{12}]^{2-}$ and $[CB_{11}H_{12}]^-$ *closo*-polyborates, we identified three key factors that can contribute to a frustrated energy landscape that inhibits cation ordering at elevated temperatures:[3,13] (1) geometric incompatibility between the anion symmetry and the lattice symmetry due to a competition between electrostatics and chemical preferences; (2) structural incompatibility due to a lack of preferred interstitial lattice sites for the cations; and (3) dynamical reorientations that lead to fluctuations in the energy landscape felt by the cations. In this section, we use our simulation

results to revisit these contributions for the title compounds while exploring additional effects specific to the introduction of the halide ion.

Figure 8b and 8e show the DFT-computed potential energy surface of a single anion-cation pair isolated from $LiHCB_{11}H_5Cl_6$. As reported previously for analogous *closo*-polyborates,[3,13] cations coordinate at the faces of the icosahedron. For the $[HCB_{11}H_5Cl_6]^-$ anion, there are four such symmetry-inequivalent faces, depicted as Ω_i in Figure 8a. The potential energy surface for a Li^+ cation moving between the faces is shown in Figures 8b and 8e alongside the analogous result for the non-halogenated $[CB_{11}H_{12}]^-$ anion in Figures 8b and 8c. Similar to the $LiCB_{11}H_{12}$ case,[13] the most energetically stable binding occurs at the face farthest from the C atom, while the face adjacent to the C atom shows no stable minimum. However, compared to $LiCB_{11}H_{12}$, the energy minima are overall shallower, particularly at faces closer to the C atom; this confirms the weaker coordinating nature of the halogenated variant. At the same time, the energy *difference* between cation binding at the three stable faces is considerably larger for $LiHCB_{11}H_5Cl_6$, with Li^+ exhibiting a stronger tendency to avoid the C atom. This means that only the halogenated side of the anion is practically accessible for cation coordination, consistent with the repulsion from the apical hydrogen atom that we concluded from Mulliken charge analysis (Figure 1). In practice, this is a consequence of the higher electronegativity of Cl relative to H, which generates a stronger dipole. As we discussed earlier, the anisotropy in the potential energy landscape should translate to an energetically stronger preference for ordering in the solid, which can explain the higher transition temperature of $LiHCB_{11}H_5Cl_6$ relative to $LiCB_{11}H_{12}$. Put another way, whereas the configurational entropy gain upon full reorientational disordering in the two materials is likely similar, the associated *enthalpy* penalty for reorientation may be higher for $[HCB_{11}H_5Cl_6]^-$ due to the larger corrugation of the anion-cation interaction energy.

Beyond the dipole effect, there is another unique factor in the cation interaction with $MHCB_{11}H_5X_6$ that derives from the polarizability of the halogen atoms. To explore this effect, we calculated the electronic polarization of the Cl atoms in $LiHCB_{11}H_5Cl_6$ using the method of maximally localized Wannier functions,[35] which were sampled from AIMD trajectories of $LiHCB_{11}H_5Cl_6$. The sum of the positions of the Wannier centers gives a measure of the polarization associated with each atom. Figures 8d and 8f compare histograms of the polarization of equivalent H and Cl atoms in $LiCB_{11}H_{12}$ and $LiHCB_{11}H_5Cl_6$, respectively. As expected, the average polarization of the Cl atoms in $LiHCB_{11}H_5Cl_6$ is much larger than the H atoms in $LiCB_{11}H_{12}$. The results become more interesting when decomposed according to the different numbers of Li^+ cations that are near the

H or Cl atom. For $LiHCB_{11}H_5Cl_6$, a clear change in the polarization as the cation coordination changes can be seen (Figure 8f), while a similar analysis of the polarization of H atoms shows no dependence on cation coordination (Figure 8d). It has previously been suggested that such fluctuations in the Li-Cl bond character dynamically alter the energy landscape, which can aid ionic conductivity by preventing cations from ordering onto a static landscape.[53] Because this effect requires larger, more polarizable halogen atoms, it can be uniquely associated with the title compounds among the existing classes of *closo*-polyborates.

The results of the potential energy landscape calculation are also validated by the AIMD simulations. Figure 8g shows the average orientations of cations around the anions in $LiHCB_{11}H_5Cl_6$ taken from AIMD simulations. Here, we have transformed the cation locations into the instantaneous rotational reference frame of the anions. In Figure 8g, local maxima in the relative probability density can be seen at polar angles θ representing icosahedral facets that are far from the C atom (e.g., Ω_3 and Ω_4 in Figure 8a). These maxima are connected by transition pathways that connect the facets along edges, avoiding the H and Cl atoms. The distributions are more diffuse at higher temperatures (Figures S41-S42, SI), but the pathways remain the same, with the motion of the cations always templated by the anion symmetry regardless of the instantaneous anion orientation.

Anion templating also governs the collective dynamics of cations around the anions, particularly at the shortest distances. This can be seen in Figure 8h, which shows the distribution of Li-anion-Li angles at three different simulation temperatures. Here, we have resolved the first coordination peak in the cation-anion pair distribution function according to cations residing closer than the peak maximum (4.2 Å) and those residing farther than the peak maximum but still within the first coordination (up to 5.7 Å) (see Supplementary Information for details). As discussed earlier, lattice symmetry analysis based on the crystal structure alone would predict a 60° Li-anion-Li angle for γ-$LiHCB_{11}H_5Cl_6$ (Figure 4b). Instead, at close distances, the distributions match the symmetry of the icosahedral anion facets (dashed lines in Figure 8h). At slightly farther distances, the 60° preference expected from crystallographic analysis finally manifests as a shoulder in the distribution. This clearly demonstrates the geometric frustration that arises from incompatible anion and lattice symmetries, similar to the behavior we previously found for high-temperature $LiCB_{11}H_{12}$.[13]

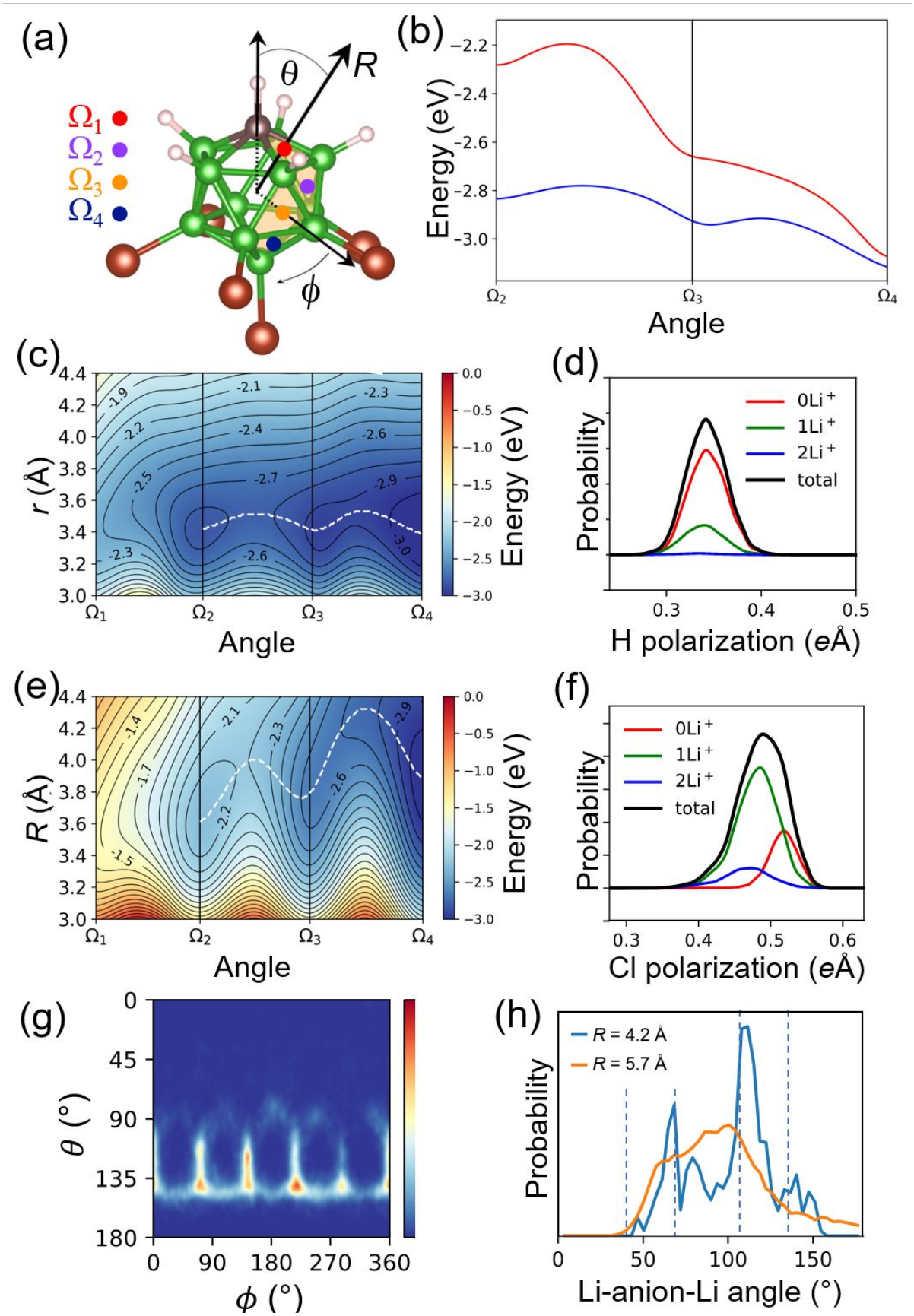
(a)
θ
R
ϕ
Ω1
Ω2
Ω3
Ω4
(b)
Energy (eV)
Angle
(c)
r (Å)
Angle
Energy (eV)
(d)
Probability
0Li+
1Li+
2Li+
total
H polarization (eÅ)
(e)
R (Å)
Angle
Energy (eV)
(f)
Probability
0Li+
1Li+
2Li+
total
Cl polarization (eÅ)
(g)
θ (°)
ϕ (°)
(h)
Probability
R = 4.2 Å
R = 5.7 Å
Li-anion-Li angle (°)

Figure 8: (a) Schematic of the $[HCB_{11}H_5Cl_6]^-$ anion, showing the polar coordinate reference frame and angles Ω_i defining the facet centers. H atoms are white, C is brown, B are dark green and Cl are brown. (b) Potential energy of a probe Li^+ cation along the minimum-energy path connecting sites at the angles Ω_i that exhibit stable minima for $[HCB_{11}H_5Cl_6]^-$ (red) versus the non-halogenated $[CB_{11}H_{12}]^-$ (blue). (c,e) Full potential energy landscapes associated with Li^+ as a function of distance from isolated (c) $[HCB_{11}H_5Cl_6]^-$ and (e) $[CB_{11}H_{12}]^-$ anions, plotted along the angular path connecting Ω_i; white dashed lines correspond to the minimum energy pathways in (b). (d,f) Histograms of the average polarization of (d) H atoms in $[CB_{11}H_{12}]^-$ and (f) Cl atoms in $[HCB_{11}H_5Cl_6]^-$ from AIMD simulations of γ-$LiHCB_{11}H_5Cl_6$ and $LiCB_{11}H_{12}$ at 500 K. Total polarization histograms (black) are further resolved according to the number of Li^+ cations in the first coordination peak (colored lines). (g) Relative probability density of angular distributions of cations around the anions of γ-$LiHCB_{11}H_5Cl_6$ within the first coordination shell from AIMD at 700 K. (h) Corresponding distributions of Li-anion-Li angles within 4.2 Å (blue) and between 4.2 Å and 5.7 Å (orange) from the anion center. Dashed lines correspond to the facet centers Ω_i.

The AIMD simulations were also used to investigate the dynamics of cation diffusion and site occupation in γ-$LiHCB_{11}H_5Cl_6$ at temperatures ranging from 500 to 1000 K. Figure 9a shows that a sharp increase in the Li diffusion coefficient occurs at $T \sim 700$ K in our simulations, indicating the onset of significant additional cation disordering. We hypothesize that this may be a signature of the superionic phase transition (the somewhat higher predicted transition temperature compared to the experimental temperature is common for AIMD). It is important to emphasize that in these simulations, we fixed the unit cells at all temperatures and no volume expansion or structural phase transformation was permitted, yet this signature of this order-disorder phase transition can still be clearly seen within the γ phase. We further tracked cation positions by mapping the cations onto the high-symmetry interstitial sites of the hexagonal anion sublattice, then recording average site occupations as a function of temperature. These results, shown in Figures 9b and 9c, show similar signatures of cation disordering beyond a threshold temperature. Li^+ cations were found to preferentially occupy linear and trigonal sites, with relative occupation of trigonal sites increasing with temperature above ~700 K (Figure 9b).

This changing site preference with temperature can be more clearly seen by separating sites into those in the (001) plane of the hexagonal unit cell, and those between planes (Figure 9c). In a unit cell with perfect *hcp* symmetry, these sites would be equivalent, but Figure 9c shows that a clear preference for sites between anion planes emerges as the temperature is increased. Overall, the fact

that we observe these signatures of the order-disorder transitions in our simulations without explicitly accounting for the structural phase transition suggests that the superionic phase transition in $LiHCB_{11}H_5Cl_6$ occurs in response to an intrinsic change in cation and anion dynamics, rather than the converse. It is also worth pointing out that even at lower temperatures, linear and trigonal sites compete with one another (Figure 9b); this indicates no strong preference for a particular type of interstitial lattice site, which was identified as another possible signature of frustration in our previous work.[3]

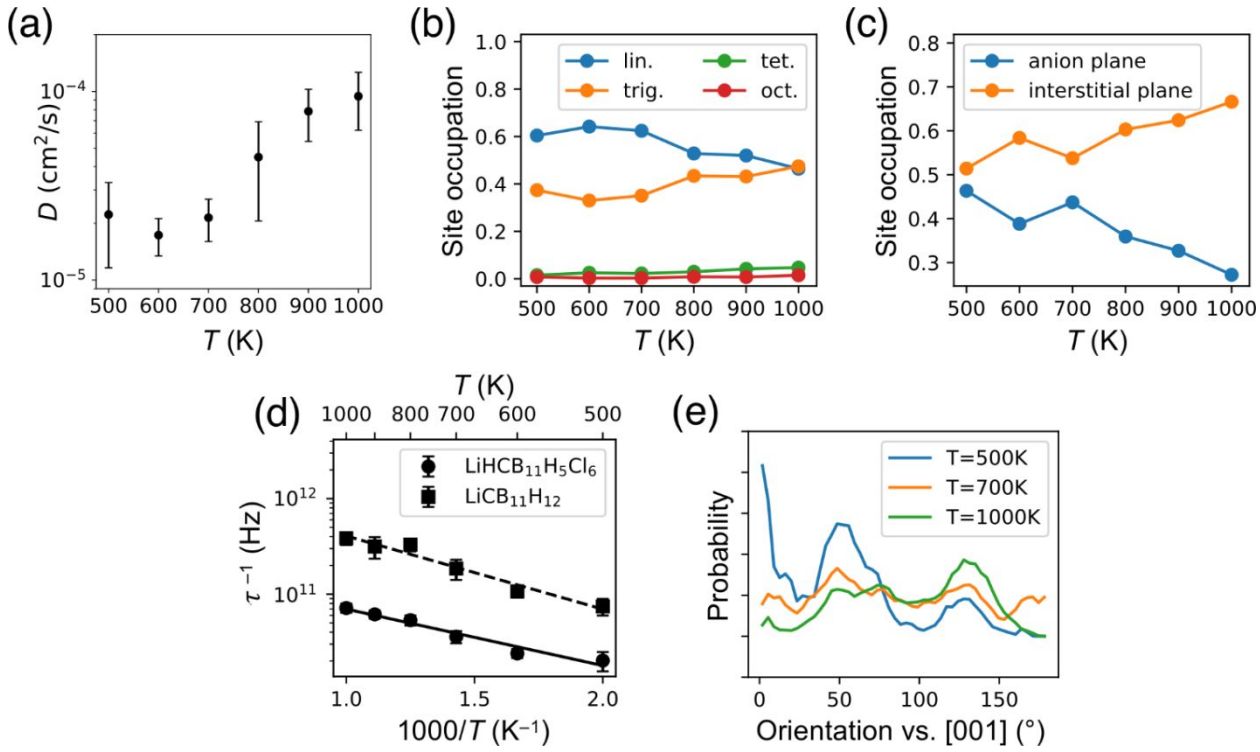

Figure 9: AIMD simulations of γ-$LiHCB_{11}H_5Cl_6$: (a) Calculated temperature-dependent Li^+ diffusion coefficient. (b) Temperature-dependent cation occupations by interstitial site geometry (linear, trigonal, tetrahedral, octahedral). See Figure 4 for definitions. (c) Relative occupations of cation sites located in the anion plane versus sites located between anion planes as a function of temperature. (d) Arrhenius plot of the calculated anion reorientation frequencies for $LiHCB_{11}H_5Cl_6$ versus $LiCB_{11}H_{12}$. Values are averaged over all molecules in the simulations, with the variance shown as error bars. (e) Relative probability distributions of the angle between the [001] crystallographic axis and the orientation of the C atom within the $[HCB_{11}H_5Cl_6]^-$ anion at three different AIMD simulation temperatures.

In addition to the cation dynamics, we also tracked the reorientational dynamics of the $[HCB_{11}H_5Cl_6]^-$-anions throughout our simulations. Anion rotation rates were extracted from the decay of the autocorrelation function for anion angular orientation with respect to the crystal axes. Compared to $[CB_{11}H_{12}]^-$, the heavier $[HCB_{11}H_5Cl_6]^-$ anions are expected to have a slower rotation rate, which is indeed seen in Figure 9d. However, if mass were the only important difference between the two anions, the rotation rate should scale as the square root of the ratio of moments of inertia (approximately 2.4 for these two anions), while the ratio of rotation rates is larger at 4-5. This suggests that, while moment of inertia is relevant, differences in anion-cation interactions may be more important for determining anion rotation rates. This is also evident from the different rates for anion reorientation observed for the geometrically similar anions in $Na_2B_{10}H_{10}$ and $NaCB_9H_{10}$.[54] Interestingly, Arrhenius fits of rotation rates give very similar energy barriers for rotations of $[HCB_{11}H_5Cl_6]^-$ (0.12 eV) compared to $[CB_{11}H_{12}]^-$ (0.15 eV) even though the rate of the former is much slower. This implies that the prefactor for anion reorientation events is decreased for $[HCB_{11}H_5Cl_6]^-$. A plausible reason for this lowered prefactor is that the lower crystallographic symmetry of $LiHCB_{11}H_5Cl_6$ compared to $LiCB_{11}H_{12}$, combined with the stronger directional preference of the $[HCB_{11}H_5Cl_6]^-$ rotations, results in fewer possible reorientation pathways for anions. Nevertheless, the reorientation dynamics are sufficiently fast to cause fluctuations in the energy landscape on the timescales of the cation motion.

It is notable that the reorientation results in Figure 9d do not exhibit any detectable signature of the transition temperature for cation disordering. Rather, the increase in rates with temperature follows a standard linear Arrhenius relation, as expected for an activated process. Accordingly, while the rotational rates of the anions may be relevant, they are insufficient to explain the sudden cation disordering observed in Figures 9a-c. However, signatures of the disorder transition do become visible when considering specific changes in anion orientational preferences with increasing temperature. These preferences are shown in Figure 9e, which plots the probability density for the angle θ of the C atom of the anions with respect to the [001] direction of the crystal. At low temperatures (e.g., 500 K), clear orientational preferences are seen, with specific ordered angles and a clear preference to orient along the [001] axis. As the temperature increases beyond the disordering temperature (~700 K in the simulations), anion orientations become more smeared out, and the reorientational dynamics transition towards more isotropic rotation. Nevertheless, a degree of

preferential orientation along the [001] axis is retained at all temperatures, which explains the decreased *c*/*a* ratio in the structure as interactions along this direction are strengthened.

Collectively, these results highlight the subtle interplay between anion symmetry, anion-cation interaction strength, and crystal symmetry in determining the phase transition temperature and ionic conductivity in these materials. For instance, if symmetry frustration between the cation-anion coordination interaction and the lattice geometry is a dominant factor coupling anion orientational disorder to cation disorder, then the strength and nature of the cation-anion interaction become especially critical.[3] Too directional an interaction leads to a high enthalpy penalty for disordering, causing a higher transition temperature. The same effect is seen if the interaction is too asymmetric, as appears to be the case with partially halogenated *closo*-carbaborate anions. On the other hand, too weak an interaction or too much symmetry leads to weaker coupling between anion and cation disorder, lessening the synergistic effect of disordering both sublattices and again leading to a higher transition temperature (seen in the $[B_{12}H_{12}]^{2-}$-based materials, as compared with the $[CB_{11}H_{12}]^{-}$-based equivalents). Rational design of properties in *closo*-polyborate-based conductors requires carefully weighing these factors to achieve the desired effect. Another successful approach for lowering the transition temperature involves mixing of different anion types in the same material.[9,11,12,16,50,55–57] The resulting intrinsic disorder in the crystal lattice has been shown to result in a lower transition temperature and higher ionic conductivity, possibly by enhancing some of the frustration effects discussed above. Another strategy is to nanoconfine such solid electrolytes inside mesoporous oxides, which has been shown to dramatically reduce the order-disorder transition temperature.[58–60]

Conclusions

In this study, we couple computational simulations and detailed structural characterization to provide fundamental insights into the factors influencing order-disorder phase transitions and ionic conductivity in Li^+ and Na^+ salts with weakly coordinating polyboron cluster anions. The *closo*-7,8,9,10,11,12-hexahalocarbaborate compounds $M(HCB_{11}H_5X_6)$ (M = Li, Na, X = Cl, Br) exhibit order-disorder phase transitions between 203 and 305 °C to form disordered hexagonal phases, with a unit cell volume expansion of approximately 10%, compared to the ordered RT phases. Above the first-order transition temperatures, all compounds exist as superionic phases with conductivity values of the order of 10^{-2} S cm^{-1} or higher, and activation energies ranging between 0.30 and 0.38 eV. The $M(HCB_{11}H_5X_6)$ compounds display order-disorder phase transitions that occur at higher temperatures

than those of the corresponding lithium and sodium $[CB_{11}H_{12}]^-$ *closo*-carbaborates, consistent with the unfavorable cation positions in the disordered phase.

DFT and *ab initio* molecular dynamics calculations reveal a lack of clear site preference for cations, evidence of geometric incompatibility between the anion symmetry and the lattice, and a changing energy landscape due to dynamic reorientations, all of which likely contribute to frustration that prevents cation ordering in the high-temperature phases. Although these features appear to be common to *closo*-polyborate ionic conductors,[3] halogen charge polarization and electronegativity play an additional important role on conductivity and order-disorder transition temperatures by affecting the cation-anion interactions and yielding a more anisotropic anion-cation potential energy surface compared to the non-halogenated $[CB_{11}H_{12}]^-$ anion.

In combination with electrochemical impedance spectroscopy and differential scanning calorimetry, the computational and structural analyses highlight the complex interdependencies in ionic conductivity and transition temperature trends observed in solid *closo*-polyborate electrolytes. Indeed, it appears that no single isolated factor can explain these trends. For instance, while the addition of halogens decreases the strength of interaction between the cation and anion, the increased inertia and size of the anion is somewhat detrimental to its reorientational mobility. Furthermore, the strict, strongly anisotropic interaction between the cation and anion appears to introduce some degree of ordering in the disordered high temperature phase. It also imposes further enthalpy costs due to the geometric mismatch between the preferred anion-cation coordination and the one imposed by the crystal symmetry. It therefore seems likely that the key to improving low-temperature ionic conductivity lies in the proper tuning of these interactions. Although some anisotropy in the cation-anion interaction appears to be beneficial for cation mobility, too directional of an interaction may instead favor ordering. Overall, the understanding afforded here suggests it may be possible to vary the number, the positions and the nature of halogen substituents (including mixed-halogen substituents), to adjust the anisotropy of the interaction and control the order-disorder phase transition, providing a valuable next step towards the rational design of solid electrolytes with tailorable properties.

Associated Content

Supporting Information: This material is available free of charge via the Internet at http://pubs.acs.org. Details on DFT and *ab initio* MD simulations and additional experimental

characterization, including NMR, FTIR, mass-spectrometry, TGA/DSC, X-ray diffraction, and Rietveld refinement results.

Author Information

Corresponding Authors: Vincent Lavallo (vincent.lavallo@ucr.edu), Torben R. Jensen (trj@chem.au.dk), Brandon C. Wood (brandonwood@llnl.gov), Vitalie Stavila (vnstavi@sandia.gov).

Notes

The authors declare no competing financial interests.

Acknowledgements

The authors gratefully acknowledge support from the Hydrogen Materials-Advanced Research Consortium (HyMARC), established as part of the Energy Materials Network under the U.S. Department of Energy, Office of Energy Efficiency and Renewable Energy, Fuel Cell Technologies Office, under Contract Number AC04-94AL85000. Sandia National Laboratories is a multi-mission laboratory managed and operated by National Technology and Engineering Solutions of Sandia, LLC., a wholly owned subsidiary of Honeywell International, Inc., for the U.S. Department of Energy's National Nuclear Security Administration under Contract No. DE-NA-0003525. A portion of this work was performed under the auspices of the U.S. Department of Energy by Lawrence Livermore National Laboratory under Contract No. AC52-07NA27344. We also gratefully thank Kyoung Kweon for useful discussions. The views and opinions of the authors expressed herein do not necessarily state or reflect those of the United States Government or any agency thereof. Neither the United States Government nor any agency thereof, nor any of their employees, makes any warranty, expressed or implied, or assumes any legal liability or responsibility for the accuracy, completeness, or usefulness of any information, apparatus, product, or process disclosed, or represents that its use would not infringe privately owned rights. The work was also supported by the Danish National Research Foundation, Center for Materials Crystallography (DNRF93), the Danish council for independent research, Nature and Universe (Danscatt), and technology and production (HyNanoBorN, DFF – 4181-00462) and the Carlsberg Foundation. Affiliation with the Center for Integrated Materials Research (iMAT) at Aarhus University is gratefully acknowledged. The authors

would like to thank the European Synchrotron Radiation Facilities (ESRF) for access to the Swiss-Norwegian beamline (BM02.1), DESY for access to Petra III, at beamline P02.1 and Diamond for access to beamline I11.

References:

(1) Chen, X.; Vereecken, P. M. Solid and Solid-Like Composite Electrolyte for Lithium Ion Batteries: Engineering the Ion Conductivity at Interfaces. *Adv. Mater. Interfaces* **2019**, *6*, 1800899.

(2) Tang, W. S.; Dimitrievska, M.; Stavila, V.; Zhou, W.; Wu, H.; Talin, A. A.; Udovic, T. J. Order–Disorder Transitions and Superionic Conductivity in the Sodium Nido - Undeca(Carba)Borates. *Chem. Mater.* **2017**, *29*, 10496–10509.

(3) Kweon, K. E.; Varley, J. B.; Shea, P.; Adelstein, N.; Mehta, P.; Heo, T. W.; Udovic, T. J.; Stavila, V.; Wood, B. C. Structural, Chemical, and Dynamical Frustration: Origins of Superionic Conductivity in Closo-Borate Solid Electrolytes. *Chem. Mater.* **2017**, *29*, 9142–9153.

(4) Tang, W. S.; Unemoto, A.; Zhou, W.; Stavila, V.; Matsuo, M.; Wu, H.; Orimo, S.; Udovic, T. J. Unparalleled Lithium and Sodium Superionic Conduction in Solid Electrolytes with Large Monovalent Cage-like Anions. *Energy Environ. Sci.* **2015**, *8*, 3637–3645.

(5) Tang, W. S.; Matsuo, M.; Wu, H.; Stavila, V.; Zhou, W.; Talin, A. A.; Soloninin, A. V.; Skoryunov, R. V.; Babanova, O. A.; Skripov, A. V.; et al. Liquid-Like Ionic Conduction in Solid Lithium and Sodium Monocarba-Closo-Decaborates Near or at Room Temperature. *Adv. Energy Mater.* **2016**, *6*, 1502237.

(6) Udovic, T. J.; Matsuo, M.; Unemoto, A.; Verdal, N.; Stavila, V.; Skripov, A. V.; Rush, J. J.; Takamura, H.; Orimo, S. I. Sodium Superionic Conduction in $Na_2B_{12}H_{12}$. *Chem. Commun.* **2014**, *50*, 3750–3752.

(7) Udovic, T. J.; Matsuo, M.; Tang, W. S.; Wu, H.; Stavila, V.; Soloninin, A. V.; Skoryunov, R. V.; Babanova, O. A.; Skripov, A. V.; Rush, J. J.; et al. Exceptional Superionic Conductivity in Disordered Sodium Decahydro-Closo-Decaborate. *Adv. Mater.* **2014**, *26*, 7622–7626.

(8) Hansen, B. R. S.; Paskevicius, M.; Li, H.; Akiba, E.; Jensen, T. R. Metal Boranes: Progress and Applications. *Coord. Chem. Rev.* **2016**, *323*, 60–70.

(9) Tang, W. S.; Yoshida, K.; Soloninin, A. V.; Skoryunov, R. V.; Babanova, O. A.; Skripov, A. V; Dimitrievska, M.; Stavila, V.; Orimo, S.; Udovic, T. J. Stabilizing Superionic-Conducting

Structures via Mixed-Anion Solid Solutions of Monocarba-Closo-Borate Salts. *ACS Energy Lett.* **2016**, *1*, 659–664.

(10) Hansen, B. R. S.; Paskevicius, M.; Jørgensen, M.; Jensen, T. R. Halogenated Sodium-Closo-Dodecaboranes as Solid-State Ion Conductors. *Chem. Mater.* **2017**, *29*, 3423–3430.

(11) Tang, W. S.; Udovic, T. J.; Stavila, V. Altering the Structural Properties of $A_2B_{12}H_{12}$ Compounds via Cation and Anion Modifications. *J. Alloys Compd.* **2015**, *645*, S200–S204.

(12) Soloninin, A. V.; Skoryunov, R. V.; Babanova, O. A.; Skripov, A. V.; Dimitrievska, M.; Udovic, T. J. Comparison of Anion and Cation Dynamics in a Carbon-Substituted Closo-Hydroborate Salt: 1H and 23Na NMR Studies of Solid-Solution $Na_2(CB_9H_{10})(CB_{11}H_{12})$. *J. Alloys Compd.* **2019**, *800*, 247–253.

(13) Dimitrievska, M.; Shea, P.; Kweon, K. E.; Bercx, M.; Varley, J. B.; Tang, W. S.; Skripov, A. V; Stavila, V.; Udovic, T. J.; Wood, B. C. Carbon Incorporation and Anion Dynamics as Synergistic Drivers for Ultrafast Diffusion in Superionic $LiCB_{11}H_{12}$ and $NaCB_{11}H_{12}$. *Adv. Energy Mater.* **2018**, *8*, 1703422.

(14) Varley, J. B.; Kweon, K.; Mehta, P.; Shea, P.; Heo, T. W.; Udovic, T. J.; Stavila, V.; Wood, B. C. Understanding Ionic Conductivity Trends in Polyborane Solid Electrolytes from Ab Initio Molecular Dynamics. *ACS Energy Lett.* **2017**, *2*, 250–255.

(15) Duchêne, L.; Lunghammer, S.; Burankova, T.; Liao, W.-C.; Embs, J. P.; Copéret, C.; Wilkening, H. M. R.; Remhof, A.; Hagemann, H.; Battaglia, C. Ionic Conduction Mechanism in the $Na_2(B_{12}H_{12})_{0.5}(B_{10}H_{10})_{0.5}$ Closo-Borate Solid-State Electrolyte: Interplay of Disorder and Ion–Ion Interactions. *Chem. Mater.* **2019**, *31*, 3449–3460.

(16) Tang, W. S.; Matsuo, M.; Wu, H.; Stavila, V.; Unemoto, A.; Orimo, S.; Udovic, T. J. Stabilizing Lithium and Sodium Fast-Ion Conduction in Solid Polyhedral-Borate Salts at Device-Relevant Temperatures. *Energy Storage Mater.* **2016**, *4*, 79–83.

(17) Reed, C. A. Carboranes: A New Class of Weakly Coordinating Anions for Strong Electrophiles, Oxidants, and Superacids. *Acc. Chem. Res.* **1998**, *31*, 133–139.

(18) Krossing, I. Coordinating Anions. *Chem. Soc. Rev.* **2016**, *45*, 789–899.

(19) Reed, C. A. H^+, CH_3^+, and R_3Si^+ Carborane Reagents: When Triflates Fail. *Acc. Chem. Res.* **2010**, *43*, 121–128.

(20) The mention of all commercial suppliers in this paper is for clarity and does not imply the recommendation or endorsement of these suppliers by NIST.

(21) Dyadkin, V.; Pattison, P.; Dmitriev, V.; Chernyshov, D. A New Multipurpose Diffractometer

PILATUS@SNBL. *J. Synchrotron Radiat.* **2016**, *23* (3), 825–829.

(22) Favre-Nicolin, V.; Černý, R. FOX, "Free Objects for Crystallography": A Modular Approach to Ab Initio Structure Determination from Powder Diffraction. *J. Appl. Crystallogr.* **2002**, *35*, 734–743.

(23) Rodríguez-Carvajal, J. Recent Advances in Magnetic Structure Determination by Neutron Powder Diffraction. *Phys. B Condens. Matter* **1993**, *192*, 55–69.

(24) Giannozzi, P.; Baroni, S.; Bonini, N.; Calandra, M.; Car, R.; Cavazzoni, C.; Ceresoli, D.; Chiarotti, G. L.; Cococcioni, M.; Dabo, I.; et al. QUANTUM ESPRESSO: A Modular and Open-Source Software Project for Quantum Simulations of Materials. *J. Phys. Condens. Matter* **2009**, *21*, 395502.

(25) Perdew, J. P.; Burke, K.; Ernzerhof, M. Generalized Gradient Approximation Made Simple. *Phys. Rev. Lett.* **1996**, *77*, 3865–3868.

(26) Car, R.; Parrinello, M. Unified Approach for Molecular Dynamics and Density-Functional Theory. *Phys. Rev. Lett.* **1985**, *55*, 2471–2474.

(27) Rappe, A. M.; Rabe, K. M.; Kaxiras, E.; Joannopoulos, J. D. Optimized Pseudopotentials. *Phys. Rev. B* **1990**, *41*, 1227–1230.

(28) Martyna, G. J.; Klein, M. L.; Tuckerman, M. Nosé–Hoover Chains: The Canonical Ensemble via Continuous Dynamics. *J. Chem. Phys.* **1992**, *97*, 2635–2643.

(29) Valiev, M.; Bylaska, E. J.; Govind, N.; Kowalski, K.; Straatsma, T. P.; Dam, H. J. J. Van; Wang, D.; Nieplocha, J.; Apra, E.; Windus, T. L.; et al. NWChem : A Comprehensive and Scalable Open-Source Solution for Large Scale Molecular Simulations. *Comput. Phys. Commun.* **2010**, *181*, 1477–1489.

(30) Kresse, G.; Furthmüller, J. Efficient Iterative Schemes for *Ab Initio* Total-Energy Calculations Using a Plane-Wave Basis Set. *Phys. Rev. B* **1996**, *54*, 11169–11186.

(31) Kresse, G.; Furthmüller, J. Efficiency of Ab-Initio Total Energy Calculations for Metals and Semiconductors Using a Plane-Wave Basis Set. *Comput. Mater. Sci.* **1996**, *6*, 15–50.

(32) Blöchl, P. E. Projector Augmented-Wave Method. *Phys. Rev. B* **1994**, *50*, 17953–17979.

(33) Feller, D. The Role of Databases in Support of Computational Chemistry Calculations. *J. Comput. Chem.* **1996**, *17*, 1571–1586.

(34) Schuchardt, K. L.; Didier, B. T.; Elsethagen, T.; Sun, L.; Gurumoorthi, V.; Chase, J.; Li, J.; Windus, T. L. Basis Set Exchange: A Community Database for Computational Sciences. *J. Chem. Inf. Model.* **2007**, *47*, 1045–1052.

(35) Marzari, N.; Mostofi, A. A.; Yates, J. R.; Souza, I.; Vanderbilt, D. Maximally Localized Wannier Functions: Theory and Applications. *Rev. Mod. Phys.* **2012**, *84*, 1419–1475.

(36) Mostofi, A. A.; Yates, J. R.; Lee, Y.; Souza, I.; Vanderbilt, D.; Marzari, N. Wannier90: A Tool for Obtaining Maximally-Localised Wannier Functions. *Comput. Phys. Commun.* **2008**, *178*, 685–699.

(37) Xie, Z.; Wu, B.; Mak, T. C. W.; Reed, C. A. Structural Diversity in Silver Salts of Hexahalogenocarborane Anions, $Ag(CB_{11}H_6X_6)$ (X = Cl, Br or I). **1997**, *640*, 1213–1217.

(38) Paskevicius, M.; Hansen, B. R. S.; Jørgensen, M.; Richter, B.; Jensen, T. R. Multifunctionality of Silver Closo-Boranes. *Nat. Commun.* **2017**, *8*, 15136.

(39) Paskevicius, M.; Pitt, M. P.; Brown, D. H.; Sheppard, D. A.; Chumphongphan, S.; Buckley, C. E. First-Order Phase Transition in the $Li_2B_{12}H_{12}$ System. *Phys. Chem. Chem. Phys.* **2013**, *15*, 15825.

(40) Verdal, N.; Her, J.-H.; Stavila, V.; Soloninin, A. V.; Babanova, O. A.; Skripov, A. V.; Udovic, T. J.; Rush, J. J. Complex High-Temperature Phase Transitions in $Li_2B_{12}H_{12}$ and $Na_2B_{12}H_{12}$. *J. Solid State Chem.* **2014**, *212*, 81–91.

(41) Sadikin, Y.; Schouwink, P.; Brighi, M.; Łodziana, Z.; Černý, R. Modified Anion Packing of $Na_2B_{12}H_{12}$ in Close to Room Temperature Superionic Conductors. *Inorg. Chem.* **2017**, *56*, 5006–5016.

(42) Wu, H.; Tang, W. S.; Zhou, W.; Stavila, V.; Rush, J. J.; Udovic, T. J. The Structure of Monoclinic $Na_2B_{10}H_{10}$: A Combined Diffraction, Spectroscopy, and Theoretical Approach. *CrystEngComm* **2015**, *17*, 3533–3540.

(43) West, A. R. Solid Electrolytes and Mixed Ionic–Electronic Conductors: An Applications Overview. *J. Mater. Chem.* **1991**, *1*, 157–162.

(44) Skripov, A. V; Skoryunov, R. V; Soloninin, A. V; Babanova, O. A.; Tang, W. S.; Stavila, V.; Udovic, T. J. Anion Reorientations and Cation Diffusion in $LiCB_{11}H_{12}$ and $NaCB_{11}H_{12}$: ^{1}H, ^{7}Li, and ^{23}Na NMR Studies. *J. Phys. Chem. C* **2015**, *119*, 26912–26918.

(45) Beniere, M.; Chemla, M.; Beniere, F. Vacancy Pairs and Correlation Effects in KCl and NaCl Single Crystals. *J. Phys. Chem. Solids* **1976**, *37*, 525–538.

(46) Friauf, R. J. Determination of Ionic Transport Processes in AgCl and AgBr. *J. Phys.* **2007**, *38*, 1077–1088.

(47) He, L.; Li, H.; Nakajima, H.; Tumanov, N.; Filinchuk, Y.; Hwang, S.; Sharma, M.; Hagemann, H.; Akiba, E. Synthesis of a Bimetallic Dodecaborate $LiNaB_{12}H_{12}$ with

Outstanding Superionic Conductivity. *Chem. Mater.* **2015**, *27*, 5483–5486.

(48) Skripov, A. V.; Babanova, O. A.; Soloninin, A. V.; Stavila, V.; Verdal, N.; Udovic, T. J.; Rush, J. J. Nuclear Magnetic Resonance Study of Atomic Motion in $A_2B_{12}H_{12}$ (A = Na, K, Rb, Cs): Anion Reorientations and Na^+ Mobility. *J. Phys. Chem. C* **2013**, *117*, 25961–25968.

(49) Duchêne, L.; Kühnel, R.-S.; Rentsch, D.; Remhof, A.; Hagemann, H.; Battaglia, C. A Highly Stable Sodium Solid-State Electrolyte Based on a Dodeca/Deca-Borate Equimolar Mixture. *Chem. Commun.* **2017**, *53*, 4195–4198.

(50) Sadikin, Y.; Brighi, M.; Schouwink, P.; Černý, R. Superionic Conduction of Sodium and Lithium in Anion-Mixed Hydroborates $Na_3BH_4B_{12}H_{12}$ and $(Li_{0.7}Na_{0.3})_3BH_4B_{12}H_{12}$. *Adv. Energy Mater.* **2015**, *5*, 1501016.

(51) Wu, H.; Tang, W. S.; Stavila, V.; Zhou, W.; Rush, J. J.; Udovic, T. J. Structural Behavior of $Li_2B_{10}H_{10}$. *J. Phys. Chem. C* **2015**, *119*, 6481–6487.

(52) Bukovsky, E. V; Peryshkov, D. V; Wu, H.; Zhou, W.; Tang, W. S.; Jones, W. M.; Stavila, V.; Udovic, T. J.; Strauss, S. H. Comparison of the Coordination of $B_{12}F_{12}^{2-}$, $B_{12}Cl_{12}^{2-}$, and $B_{12}H_{12}^{2-}$ to Na^+ in the Solid State: Crystal Structures and Thermal Behavior of $Na_2(B_{12}F_{12})$, $Na_2(H_2O)_4(B_{12}F_{12})$, $Na_2(B_{12}Cl_{12})$, and $Na_2(H_2O)_6(B_{12}Cl_{12})$. *Inorg. Chem.* **2017**, *56*, 4369–4379.

(53) Adelstein, N.; Wood, B. C. Role of Dynamically Frustrated Bond Disorder in a Li^+ Superionic Solid Electrolyte. *Chem. Mater.* **2016**, *28*, 7218–7231.

(54) Soloninin, A. V; Dimitrievska, M.; Skoryunov, R. V; Babanova, O. A.; Skripov, A. V; Tang, W. S.; Stavila, V.; Orimo, S.; Udovic, T. J. Comparison of Anion Reorientational Dynamics in MCB_9H_{10} and $M_2B_{10}H_{10}$ (M = Li, Na) via Nuclear Magnetic Resonance and Quasielastic Neutron Scattering Studies. *J. Phys. Chem. C* **2017**, *121*, 1000–1012.

(55) Kim, S.; Oguchi, H.; Toyama, N.; Sato, T.; Takagi, S.; Otomo, T.; Arunkumar, D.; Kuwata, N.; Kawamura, J.; Orimo, S. A Complex Hydride Lithium Superionic Conductor for High-Energy-Density All-Solid-State Lithium Metal Batteries. *Nat. Commun.* **2019**, *10*, 1081.

(56) Brighi, M.; Murgia, F.; Łodziana, Z.; Schouwink, P.; Wołczyk, A.; Cerny, R. A Mixed Anion Hydroborate/Carba-Hydroborate as a Room Temperature Na-Ion Solid Electrolyte. *J. Power Sources* **2018**, *404*, 7–12.

(57) Yoshida, K.; Sato, T.; Unemoto, A.; Matsuo, M.; Ikeshoji, T.; Udovic, T. J.; Orimo, S. Fast Sodium Ionic Conduction in $Na_2B_{10}H_{10}$-$Na_2B_{12}H_{12}$ Pseudo-Binary Complex Hydride and Application to a Bulk-Type All-Solid-State Battery. *Appl. Phys. Lett.* **2017**, *110*, 103901.

(58) Cuan, J.; Zhou, Y.; Zhou, T.; Ling, S.; Rui, K.; Guo, Z.; Liu, H.; Yu, X. Borohydride-Scaffolded Li/Na/Mg Fast Ionic Conductors for Promising Solid-State Electrolytes. *Adv. Mater.* **2019**, *31*, 1803533.

(59) Blanchard, D.; Nale, A.; Sveinbjörnsson, D.; Eggenhuisen, T. M.; Verkuijlen, M. H. W. W.; Suwarno; Vegge, T.; Kentgens, A. P. M. M.; De Jongh, P. E. Nanoconfined $LiBH_4$ as a Fast Lithium Ion Conductor. *Adv. Funct. Mater.* **2015**, *25*, 184–192.

(60) Yan, Y.; Rentsch, D.; Battaglia, C.; Remhof, A. Synthesis, Stability and Li-Ion Mobility of Nanoconfined $Li_2B_{12}H_{12}$. *Dalton Trans.* **2017**, *46*, 12434–12437.

TOC Figure